Applied Geochemistry 182 (2025) 106302

Contents lists available at ScienceDirect

Applied Geochemistry

journal homepage: www.elsevier.com/locate/apgeochem

Structural characterization of amorphous hydrous Zr(IV) oxide and the transformation occurring under hydrothermal conditions

Christian Kiefer [a,b,*], Xavier Gaona [a,**], Tomo Suzuki-Muresan [b,***], Dieter Schild [a], Krassimir Garbev [c], Taishi Kobayashi [d], Kathy Dardenne [a], Oliver Dieste Blanco [a], Marcus Altmaier [a], Bernd Grambow [b], Horst Geckeis [a]

[a] Karlsruhe Institute of Technology, Institute for Nuclear Waste Disposal, Karlsruhe, Germany
[b] SUBATECH – IMT Atlantique, Université de Nantes, CNRS/IN2P3, Nantes, France
[c] Karlsruhe Institute of Technology, Institute for Technical Chemistry, Karlsruhe, Germany
[d] Department of Nuclear Engineering, Kyoto University, Kyoto, Japan

ARTICLE INFO

Editorial handling by: Dr Mavrik Zavarin

Keywords:
Zirconium
ZrO_2
Amorphous
crystalline
Transformation
$CaCl_2$
Multimethod approach

ABSTRACT

The impact of temperature on the transformation of ZrO_2(am, hyd) in aqueous systems was systematically investigated using a multi-method approach for solid phase characterization. Ageing at $T = 80$ °C in NaOH and alkaline $CaCl_2$–$Ca(OH)_2$ solutions triggered the conversion of ZrO_2(am, hyd) to more crystalline, thermodynamically stable anhydrous oxides. Compared to the fresh amorphous solid and solids aged at $T = 22$ °C, an increase in crystallinity and particle size accompanied by a significant decrease in the amount of hydration water or hydroxide was observed. After equilibration for 4 or 10 months at T = 80 °C, XRD measurements confirmed the predominance of monoclinic ZrO_2 with a particle size of 23–27 nm in NaOH systems, whereas tetragonal/cubic ZrO_2 with a particle size of 11–14 nm formed in $CaCl_2$–$Ca(OH)_2$ solutions. All solids aged at $T = 22$ °C remained X-ray amorphous within the timeframe of this study. Rietveld refinement of the XRD patterns, EDX and EXAFS supported that the stabilization of a different crystal structure in $CaCl_2$–$Ca(OH)_2$ systems is caused by the incorporation of Ca^{2+} in the ZrO_2 structure. The weight loss observed with TG-DTA was attributed to a decreasing amount of hydration water during the ageing at $T = 80$ °C. Assuming a stoichiometry of $ZrO_2{\cdot}nH_2O$, the fresh solid showed a weight loss corresponding to $n = 2.1$, which remained constant during the ageing at $T = 22$ °C. The solids aged at $T = 80$ °C showed a smaller weight loss corresponding to $n = 0.2$–0.6. This behavior was qualitatively confirmed by IR-ATR. XPS analysis of the O1s line also showed a decrease of H_2O/OH^- contributions and an increase of O^{2-} contributions in the solid phases aged at $T = 80$ °C.

This study provides new insights for the understanding of the transformation of M(IV) amorphous, hydrous oxides into the thermodynamically stable anhydrous crystalline oxide phases. The process involves particle growth, increased ordering and loss of H_2O/OH^- groups. In aqueous systems, the presence of other metal ions like Ca^{2+} may promote the stabilization of different crystal structures, even if they are found at low concentrations.

1. Introduction

Zirconium alloys are used as cladding material for nuclear fuel, especially in water cooled reactors (Kobayashi et al., 2013; Northwood, 1985). ^{93}Zr ($t_{1/2} = 1.53{\cdot}10^6$ a (Macklin, 1985)) is produced by nuclear fission of ^{235}U as well as by neutron activation of stable Zr in the cladding (Metz et al., 2012). In the case of early canister failure, Zr-containing waste could come into contact with water (Metz et al., 2012). This scenario would lead to the formation of hydrous zirconium oxides, which are expected to be the Zr(IV) solubility controlling solid

This article is part of a special issue entitled: Migration 2023 published in Applied Geochemistry.

* Corresponding author. Karlsruhe Institute of Technology, Institute for Nuclear Waste Disposal, Karlsruhe, Germany.
** Corresponding author. Karlsruhe Institute of Technology, Institute for Nuclear Waste Disposal, Karlsruhe, Germany.
*** Corresponding author. SUBATECH – IMT Atlantique, Université de Nantes, CNRS/IN2P3, Nantes, France.
E-mail addresses: christian.kiefer2@kit.edu (C. Kiefer), xavier.gaona@kit.edu (X. Gaona), suzuki@subatech.in2p3.fr (T. Suzuki-Muresan).

https://doi.org/10.1016/j.apgeochem.2025.106302
Received 15 July 2024; Received in revised form 3 February 2025; Accepted 8 February 2025
Available online 16 February 2025

phases (Brown et al., 2005; Kobayashi et al., 2013). Depending on several factors like temperature, pH or present background ions, these solid phases are expected to undergo crystallization processes towards thermodynamic more stable modifications by dissolution/precipitation mechanisms (Štefanić et al., 1997, 2005). Since the properties (e.g., crystallinity, particle size, hydration degree) of these solid phases significantly affect solubility and thus mobility of the radionuclides (Kobayashi et al., 2013), it is of greatest importance to investigate these processes.

Temperature is one of the parameters that will vary during the different phases of operation of a repository for high-level radioactive waste (HLW). Elevated temperatures (depending upon waste type, repository concept and host-rock system) will affect the chemistry in the near-field in the case of early canister failure (Metz et al., 2012).

The use of cementitious materials in several repository concepts can lead to a significant increase in Ca concentrations (0.02 M Ca) and buffering the pH of the system in alkaline regions (up to pH = 12.5), in equilibrium with calcium silicate hydrate (C–S–H) phases and portlandite ($Ca(OH)_2$(cr)). Moreover, in brine solutions containing high concentrations of $MgCl_2$, cement has been shown to leach large fractions of Ca, resulting in pore water solutions with high Ca content (i.e., up to 2.0 M) at pH ≈ 12 (Bube et al., 2013).

Tetravalent metals M(IV) have a strong tendency to hydrolyse in aqueous solutions. Cationic hydrolysis species, $M_x(OH)_y^{4x-y}$ (with $y < 4x$), are expected to control the aqueous speciation of M(IV) under highly acidic conditions, whereas the neutral species $M(OH)_4$(aq) (or analogous neutral polynuclear moieties) predominates from acidic to alkaline pH conditions (Altmaier et al., 2013). For some tetravalent transition metals (e.g. Zr, Tc) the predominance of anionic hydrolysis species $M(OH)_y^{4-y}$ or $MO(OH)_z^{2-z}$ (with $y > 4$ and $z > 2$) is reported in hyperalkaline pH systems (Brown et al., 2005; Grenthe et al., 2020). Besides their strong hydrolysis, M(IV) metal ions are also characterized by the formation of sparingly soluble amorphous hydrous oxides, MO_2(am, hyd), which control M(IV) solubility over a broad range of pH from acidic to hyperalkaline conditions. The transition of these amorphous solids, MO_2(am, hyd), into the thermodynamically more stable crystalline phases MO_2(cr) is kinetically hindered and is generally not observed in short-term laboratory experiments involving aqueous systems. The ageing or exposure of these solid phases to elevated temperatures expectedly results in increased crystallinity (*i.e.* particle size), and thus in a decreased solubility in aqueous systems (Kobayashi et al., 2013, 2016a; Nishikawa et al., 2018; Rai et al., 2000).

Crystalline ZrO_2 is known to form three different polymorphs. The naturally occurring solid phase stable at low temperature shows a monoclinic structure, whereas tetragonal and cubic crystal structures are observed above T = 1447 K and 2566 K, respectively (Brown et al., 2005). The addition of a few percent of lanthanide oxides promotes the stabilization of the high-temperature polymorphs at lower temperatures (Brown et al., 2005). This effect is caused by the distortion of the Zr–O polyhedra by creation of vacancies or the inclusion of over or undersized cations (Li et al., 1993a, 1993b, 1994a, 1994b). A similar behavior is also known for Ca, which can stabilize both the tetragonal (1–5 mol% CaO) and the cubic (7+ mol% CaO) crystal structures (Dell'Agli and Mascolo, 2000). The low temperature formation of calcium zirconate ($CaZrO_3$) and other sub-stoichiometric ternary oxides was also previously shown (Li et al., 2007; Stubican and Ray, 1977). While $CaZrO_3$ is conventionally synthesized by a solid-solid reaction of ZrO_2 and $CaCO_3$ at temperatures higher than 1300 °C, Li and co-workers were able to synthesize $CaZrO_3$ from molten salts out of $CaCl_2$, Na_2CO_3 and ZrO_2 at 700 °C (Li et al., 2007). Sub-stoichiometric compounds as $CaZr_4O_9$ can be found at lower temperatures and with lower CaO mol% (Stubican and Ray, 1977). Even if such high temperatures and Ca concentrations are not expected in nuclear waste repositories, the long storage time, the possible presence of Ca and the expectedly higher reactivity of amorphous hydrous zirconium oxides compared to crystalline ZrO_2 opens the possibility of ternary Ca–Zr-oxides formation under repository-relevant conditions.

On the other hand, the poorly crystalline solid phases expected to control the solubility of Zr(IV) in aqueous systems remain ill-defined, as well as the mechanism and kinetics for the transformation into ZrO_2(cr). Pitcher et al. investigated nanocrystalline tetragonal, monoclinic and amorphous ZrO_2 solids with different specific surface areas by high-temperature oxide melt solution calorimetry in order to measure surface enthalpies of the solids (Pitcher et al., 2005). This resulted in phase transition enthalpies and a stability map for ZrO_2, showing stability crossovers from monoclinic (thermodynamically most stable phase for solids with a surface area <2500 m^2/mol or > 48 nm particle size, respectively), to tetragonal (2500–15000 m^2/mol, 9–48 nm), and eventually to amorphous (>15000 m^2/mol, <9 nm) solid phases with increasing surface area, and thus decreasing particle size. More recently, Sharma and co-workers proposed a new stability map for ZrO_2 calculated on the basis of enthalpy data from previous experiments (Sharma et al., 2018). These calculations show amorphous (<3 nm), cubic (3–6 nm), tetragonal (6–48 nm) and monoclinic (>48 nm) ZrO_2 as thermodynamically most stable phases for each particle size regime.

Kobayashi and co-workers (Kobayashi et al., 2013, 2016b, 2019) investigated the effect of temperature (T = 323–363 K) on the solubility and structure of Zr(IV) amorphous hydrous oxide, ZrO_2(am, hyd). X-ray diffraction (XRD) and transmission electron microscopy (TEM) measurements showed the agglomeration and crystallization with increasing temperature towards thermodynamic more stable solid phases, accompanied by a clear decrease of the solubility after ageing at 363 K (Kobayashi et al., 2013). Recently, Kobayashi et al. investigated the effect of temperature on the solubility and structure of ZrO_2(am, hyd) by means of wide-angle X-ray scattering (WAXS), small-angle X-ray scattering (SAXS), extended X-ray absorption fine structure (EXAFS) and TEM techniques. The authors demonstrated that solid phases aged at T = 298 K contain hierarchical structures of aggregates of primary particles built of zirconium hydroxide tetramers and dimers. Investigations with solid phases aged at T = 298, 313, 333 and 363 K at different pH values show that these hierarchical structures are stable up to 333 K under acidic and neutral conditions and up to 313 K under alkaline conditions. By ageing at T = 363 K in acidic media and at 333 and 363 K under alkaline conditions, the formation of crystalline solids with lower solubility was described (Kobayashi et al., 2019). Although less investigated for the Zr(IV) system, the transformation of M(IV) hydrous oxides into the crystalline counterparts expectedly involves the release of water, either as a result of the condensation of OH-groups, or through the desorption of chemisorbed and physisorbed water molecules (Cevirim-Papaioannou, 2018; Grenthe et al., 2020; Kiefer et al., 2022; Rothe et al., 2002, 2004).

The hydrothermal ageing of amorphous zirconium oxide solid phases was previously investigated by Štefanić and co-workers (Štefanić et al., 1997, 2005), who performed kinetic calorimetric and XRD studies of zirconia and hafnia samples. Their experiments cover various conditions, e.g. acidic (2/ 3), neutral (7), alkaline (9.5) and hyperalkaline (13) pH conditions, different ageing temperatures (90, 95, and 120 °C) and ageing times from only a few hours up to 2 months. The authors show by XRD and Raman analysis a transformation from amorphous to crystalline ZrO_2 solid phases within a few days for samples in acidic and hyperalkaline conditions, while the alkaline and neutral samples stay amorphous or need longer hydrothermal ageing times to transform (Štefanić et al., 1997). Their more systematic study on hafnia (Štefanić et al., 2005) shows the transformation to monoclinic hafnia under all conditions, also with faster transformation kinetic for acidic and hyperalkaline conditions and at 120 °C compared to 90 °C. However, most of their aged samples contain mixtures of crystalline and amorphous solid phases, from which the latter ones even with low percentages could be solubility controlling with regard to nuclear waste repositories. Opitz and co-workers (Opitz et al., 2023) investigated the incorporation of Eu^{3+} and Cm^{3+} into zirconia by co-precipitation and subsequent hydrothermal ageing at pH 12 and T = 80 °C. The authors

showed that the crystallization of amorphous zirconia already starts after 10 days and results in mainly monoclinic with smaller contributions of tetragonal and cubic ZrO_2.

The present study systematically investigates the impact of temperature on the particle size, crystallinity and water content of ZrO_2(am, hyd) solid phases. Ageing in aqueous media is performed in NaOH and $CaCl_2$–$Ca(OH)_2$ systems in order to assess the impact of different counterions in the crystallization process. The range of pH and Ca concentrations considered in this study embraces those developing in cementitious systems, as usually considered in repository concepts for low and intermediate level waste (L/ILW) or (in specific cases, e.g., the supercontainer concept in Belgium (Craeye et al., 2009)) high level waste. A multi-method approach covering a broad range of analytical techniques is used for solid phase characterization, including XRD, TEM, scanning electron microscopy with energy dispersive X-ray spectroscopy (SEM-EDS), Raman spectroscopy, SAXS, EXAFS, thermogravimetric analysis with differential thermal analysis (TG-DTA), Fourier-transform infrared spectroscopy (FTIR), X-ray photoelectron spectroscopy (XPS), ζ-potential measurements and Brunauer-Emmett-Teller (BET) surface area analysis. As overarching objective, this work intends to shed light on the mechanisms for the potential transformation of X-ray amorphous hydrous oxides into thermodynamically more stable crystalline phases of Zr(IV) relevant in the context of nuclear waste disposal.

2. Experimental

2.1. Chemicals

Zirconium dichloride oxide hydrate ($ZrOCl_2{\cdot}xH_2O$, 99.99%) was purchased from AlfaAesar. Commercial ZrO_2(cr) was obtained from Sigma Aldrich. Sodium chloride (NaCl), calcium chloride ($CaCl_2$), nitric acid (ultrapure), HCl Titrisol© and NaOH Titrisol© were purchased from Merck. Ethanol (99.9%) was obtained from VWR Chemicals.

All solutions were prepared with Milli-Q water (Milli-Q academic, Millipore, 18.2 MΩ cm). Before use, Milli-Q water was purged with Ar for >1 h to remove traces of dissolved CO_2(g). All samples were prepared and stored in an Ar-glove box (<1 ppm O_2), either at $T = 22$ or 80 °C.

2.2. Solid phase preparation and ageing

The starting solid phase, ZrO_2(am, hyd, fresh) (sample name: fresh), was prepared by slow titration of 0.02 M $ZrOCl_2$ solution with 0.1 M NaOH. Different aliquots of the freshly precipitated solid phase were aged at $T = 80$ °C in 0.2 M $CaCl_2$–$Ca(OH)_2$, 0.02 M $CaCl_2$–$Ca(OH)_2$ or 0.001 M NaOH solutions at $pH_m = 11.0$ (with $pH_m = -\log [H^+]$), after washing 3–4 times with the corresponding solution (samples: m4Ca80, m4_002Ca80, m10Ca80, m4Na80, m10Na80). The amount of ZrO_2(am, hyd, fresh) used for each sample corresponds to ≈ 1.2 g of pure anhydrous ZrO_2. With 200 ml of background electrolyte this resulted in solid to liquid ratios of ≈ 6 g/l, assuming pure ZrO_2 instead of a wet amorphous precipitate. The Ca concentrations of 0.2 and 0.02 M lead to Ca:Zr ratios of ≈ 4:1 (0.2 M Ca) and ≈ 1:2.5 (0.02 M Ca) in the complete system. Ageing experiments were conducted for contact times of 4 and 10 months. Additional samples were aged for t = 10 months at T = 22 °C (in 0.2 M $CaCl_2$–$Ca(OH)_2$ and 0.001 M NaOH) (samples: m10Ca22, m10Na22). Another aliquot of the freshly precipitated solid phase was washed with water and aged at $T = 80$ °C without addition of a background electrolyte (m10noH_2O80). The authors note that this solid phase, due to its initial state as amorphous hydrous solid, potentially released small quantities of water during the ageing process, which could eventually contribute to the recrystallization process. After the corresponding contact time, samples aged at $T = 80$ °C were cooled down to $T = 22$ °C under Ar atmosphere. The solid phases were separated from the supernatant solution by centrifugation and were washed 2–3 times with water. Untreated commercial ZrO_2(cr) powder (sample name: crystalline) was used for comparison with the fresh and aged samples. This solid was not exposed to elevated temperatures and only washed/contacted with aqueous solutions or ethanol when necessary for the characterization methods. An overview of the investigated solids and the characterization techniques is shown in Table 1.

2.3. pH measurements

pH measurements were conducted with a ROSS pH combination electrode (Thermo Scientific, OrionTM). The electrode was calibrated with standard buffer solutions (pH = 2, 6, 8, 12). In aqueous solutions with ionic strength ≥0.1 mol kg^{-1}, pH measurements are affected by the changes in the activity coefficient of hydrogen ions (due to ion interactions) and also by the liquid junction potential of the electrode, E_j. For this reason, the hydrogen ion concentration was instead calculated as pH_m (molal scale) with $pH_m = pH_{exp} + A_m$, where pH_{exp} is the experimentally measured pH, A_m is a correction factor entailing both the activity coefficient of H^+ and the liquid junction potential of the electrode (E_j) in a given background electrolyte and background electrolyte concentration. Values of A_m in NaCl and $CaCl_2$ solutions were taken from Altmaier et al. (Altmaier et al., 2003, 2008).

2.4. Solid characterization

As summarized in Table 1, the fresh, the aged and the commercial solid phases were characterized using a multi-method approach. Powder XRD and Rietveld analysis of the obtained diffractograms were performed with the aim of determining and quantifying the crystal modifications present in the solid phases. TEM and SEM-EDS analysis were used to investigate the particle size and shape. Additionally, the EDS provides information about the elemental composition of the samples. For a more detailed characterization of the structure of the solids, Raman spectroscopy, SAXS and EXAFS measurements were conducted. TG-DTA, FTIR and XPS analysis were performed in order to investigate the H_2O/OH content in the solid phases and ζ-potential and BET measurements to asses surface properties of the solid phases. The devices, measurement conditions and sample preparations for these methods are described in the following chapters 2.4.1 to 2.4.5.

2.4.1. XRD and rietveld analysis

The crystallinity and phase composition of the aged ZrO_2 solid phases were evaluated by XRD with a Bruker AXS D8 Advance X-ray powder diffractometer (Cu-Kα radiation, LynxEye XE-T detector) for all solids. Diffraction patterns were collected for $2° < 2\theta < 70°$, with incremental steps of 0.015° and a measurement time of 0.4 s/step. Aliquots with approximately 1–2 mg of each solid phase were washed 3 times with 0.5 ml of ethanol to remove the matrix solutions. After the last washing step, the solid phase was re-suspended in ethanol, deposited on a sample holder and dried under Ar atmosphere. Diffractograms collected were compared with reference data reported in the Crystallography Open Database (COD) (Downs and Hall-Wallace, 2003; Gražulis et al., 2009, 2012, 2015; Merkys et al., 2016, 2023; Quirós et al., 2018; Vaitkus et al., 2021). Based on the full width at half maximum (FWHM) of the diffraction peaks, the crystallite size for a given solid was calculated using the Scherrer equation (Scherrer, 1918). For selected solid phases, Rietveld refinements were performed with TOPAS v. 7 (Bruker-AXS, Karlsruhe, Germany) using fundamental parameters approach. ICSD Nr. 47803 was used as initial structure data for monoclinic ZrO_2 (Sirotinkin et al., 2022b). The data from Fábregas et al. (2008) (Fábregas et al., 2008) which are similar to that of Rabenau (1956) and Morinaga and co-workers (Morinaga et al., 1979) for Ca substituted ZrO_2 and those of Bouvier et al. (2001) (Bouvier et al., 2001) were used as starting models for the cubic and tetragonal structures, respectively. The occupancy of the 4a Wyckoff position in the *Fm-3m* structure (0.0.0) was refined for Ca substitution of Zr with a constraint $S = Zr_{occ} + Ca_{occ} = 1.00$. Correspondingly, the occupancy of the oxygen

Table 1
Overview of the investigated solid phases, experimental conditions and characterization methods considered in this study.

Sample name[a]	Ageing time (days)	Ageing T (°C)	Background electrolyte (pH = 11)	XRD	TEM	SEM-EDS	Raman	SAXS	EXAFS	TG-DTA	FTIR	XPS	ζ-potential	BET
fresh	–	–	–	x	x	x		x	x	x	x	x	x	
m10Ca22	279	22	0.2 M $CaCl_2$	x	x	x	x	x	x	x	x	x		x
m10Na22	279	22	0.001 M NaOH	x	x	x	x	x	x	x	x	x		x
m4Ca80	125	80	0.2 M $CaCl_2$	x	x	x		x	x	x	x	x	x	x
m4_002Ca80	116	80	0.02 M $CaCl_2$	x	x	x	x	x	x	x	x	x		
m10Ca80	279	80	0.2 M $CaCl_2$	x	x	x	x	x	x	x	x	x	x	
m4Na80	125	80	0.001 M NaOH	x	x	x		x	x	x	x	x	x	
m10Na80	279	80	0.001 M NaOH	x	x	x	x	x	x	x	x	x	x	
m10noH_2O80	273	80	No liquid phase	x	x	x	x	x	x	x	x	x	x	x
crystalline	–	–	–	x	x	x	x	x	x	x	x	x	x	x

[a] For each sample, "mX" indicates X months of ageing, "Ca, Na, _002Ca, noH_2O" shows the ageing conditions, 22 or 80 shows the ageing temperature in °C.

position (8c) (1/4, 1/4, 1/4) was constrained to $O_{occ} = 1\text{-}(Ca_{occ}/2)$ in order to maintain the charge balance. In all cases, preferred orientation along 111 and 200 directions in the cubic structure were considered. Independent refinement of the thermal parameters (B_{iso}) was performed considering fixed occupancy, due to possible structure disorder. The size of coherent scattering domains was determined by the double Voigt approach.

2.4.2. TEM, SEM-EDS and Raman

TEM measurements were performed with a FEI Tecnai G2 operated at 200 kV available at the Fusion Laboratory of the Institute for Applied Materials at KIT. The microscope is equipped with an in-situ Gatan Tridiem Camera that provides high quality imaging and an Energy Dispersive X-ray Spectroscopy detector (EDS). Electron diffractions obtained from the sample were analyzed and compared making use of the Process Diffraction software (Lábár, 2008). A few μL of the solids suspended in ethanol were deposited on a TEM grid and dried under Ar atmosphere.

A FEI Quanta 650 FEG environmental scanning electron microscope was used to image the carbon coated sample surfaces. Scanning electron microscopy (SEM) coupled with energy-dispersive X-ray spectroscopy (EDX) was done with a Thermo Fisher Scientific UltraDry, i.e. Peltier cooled, silicon drift X-ray detector. The primary electron beam energy was 15 keV.

For XPS, SEM-EDX and Raman, solid phases were re-suspended in ethanol and deposited on a piece of indium foil and dried under Ar atmosphere before transferring the sample to the corresponding equipment.

Raman spectroscopy measurements were done with a Bruker Senterra II Raman microscope with 532 and 785 nm lasers and a spectral resolution of 1.5 cm^{-1}.

2.4.3. SAXS and EXAFS

SAXS measurement were conducted at the Aichi Synchrotron Radiation Center, Japan, using an X-ray wavelength (λ) of 0.092 nm with a wavelength distribution of $\lambda/\Delta\lambda \gg 2000$. The scattering vector q ($q = 4\pi\sin\theta/\lambda$) was $0.06 < q\ [nm^{-1}] < 12.0$, where 2θ is the scattering angle. This corresponds to a size range of $105 > D\ [nm] > 0.52$, where $D = 2\pi/q$. Small portions of the dried solids were loaded either in a glass capillary or in a sample cell covered by quartz glass (20 μm thickness).

EXAFS measurements were performed at the INE beamline at the KIT Light Source (Karlsruhe, Germany) (Rothe et al., 2012, 2019; Zimina et al., 2017). About 10–15 mg of each washed solid phase were re-suspended in a small volume of water, dried under Ar atmosphere to a wet paste and placed into a gas-tight plastic cell. The plastic cells were mounted in an air-tight sample holder and transported to the synchrotron source, where they were stored and measured under Ar atmosphere. The resulting EXAFS spectra were processed using Athena and Artemis software from the Demeter software package (Ravel and Newville, 2005).

2.4.4. TG-DTA, FTIR and XPS

TG-DTA was performed under Ar atmosphere using a Netzsch STA 449C equipment. Measurements were performed with 10–20 mg of solid material, washed with ethanol and dried under Ar atmosphere at room temperature for several days. Samples were heated up to 1200 °C with a heating rate of 10 K min^{-1}.

FTIR measurements were performed with a Bruker Optics Invenio R FTIR spectrometer equipped with a Platinum ATR accessory A225/QI-I single reflection diamond crystal and a DLaTGS detector with a spectral resolution of 4 cm^{-1}. A few mg of each solid were dried under Ar atmosphere and placed on the ATR diamond crystal. The measurements took place under air conditions. OPUS software (Bruker Optics) was used to operate the device and evaluate the data.

XPS measurements were performed with a PHI 5000 VersaProbe II (ULVAC-PHI Inc.) XPS system equipped with a scanning microprobe X-ray source (monochromatic Al Kα, $h\nu = 1486.7$ eV). For charge compensation at isolating samples, low energy argon ions (8 eV) generated by a floating ion gun and low energy electrons (1.1 eV) generated by an electron flood gun were applied (dual beam technique). The angle between analyzer and sample surface was 45°. Survey scans were recorded with a pass energy of the analyzer of 187.85 eV. Narrow scans of the elemental lines were recorded with 23.5 eV pass energy. After taking into account sensitivity factors, the transmission function of the analyzer, asymmetry parameters of elemental lines and removal of a local Shirley background, atomic concentrations can be calculated with a relative error of ± (10–20) % using the areas of elemental lines of the survey spectra. Gaussian curve fits to narrow scans of O 1s elemental lines were performed after Shirley background subtraction in order to determine the speciation of the oxygen atoms (O^{2-}, OH^- or H_2O). Data analysis was performed using ULVAC-PHI MultiPak program, version 9.9.

2.4.5. ζ-potential and BET

Electrophoretic mobility measurements were performed with a Brookhaven Instruments NanoBrook 90Plus PALS device. The measured mobilities were converted to ζ-potentials by the internal software of the device using the Smoluchovsky equation. Suspensions with 0.1 g/L of the solids were prepared in 1 mM HCl–NaCl–NaOH and 1 mM HCl–$CaCl_2$–$Ca(OH)_2$ under Ar atmosphere. The pH was adjusted to approximately 3.0, 4.5, 6.0, 8.0, 9.5 and 11.0 for each system. Each ζ-potential measurement consists of 10 averaged runs, in each of the runs 30 mobility/ζ-potential values were determined.

BET measurements were done with a 3P Instruments Sync440A device with nitrogen as adsorbate. 300, 500 or 1000 mg of selected solids (depending on the expected surface area and the available amount of substance) were dried under Ar atmosphere first and afterwards outgassed for 10 h at 80 °C to avoid residues of water or gases.

3. Results and discussion

3.1. Structure and particle size

3.1.1. XRD and rietveld analysis

Fig. 1 shows the XRD patterns of ZrO_2(s) solid phases aged for 4 and 10 months in 0.001 M NaOH, as well as in 0.02 and 0.2 M $CaCl_2$ solutions adjusted to pH_m = 11. The figure includes also the patterns collected for the freshly precipitated and crystalline solid phases, i.e, ZrO_2(am, hyd, fresh) and ZrO_2(cr).

The diffractogram of the freshly precipitated ZrO_2(am, hyd, fresh) is characterized by the lack of any reflections, which confirms the X-ray amorphous character of the material. Similarly, solids aged for 10 months at T = 22 °C (m10Na22, m10Ca22) do not present any diffraction patterns. However, after 4 and 10 months of equilibration time at *T* = 80 °C, the aged solid phases show broad but well-defined patterns in agreement with references for monoclinic, tetragonal or cubic ZrO_2(cr) available in the COD database (Downs and Hall-Wallace, 2003; Gražulis et al., 2009, 2012, 2015; Merkys et al., 2016, 2023; Quirós et al., 2018; Vaitkus et al., 2021). The solid phases aged in NaOH (Fig. 1, red diffractograms) solutions, aged without liquid phase and the commercial crystalline solid phase (Fig. 1, black) show main reflections at 2θ = 24.2, 28.1, 31.5, 34.2, 35.3 and 50.1° agreeing well with reference patterns of monoclinic ZrO_2 (Fig. 1, orange) (Downs and Hall-Wallace, 2003; Gražulis et al., 2009, 2012, 2015; Merkys et al., 2016, 2023; Quirós et al., 2018; Vaitkus et al., 2021). A reflection at 2θ = 30.2°, also present in some of these diffractograms indicates a small contribution of the cubic/tetragonal structure (Downs and Hall-Wallace, 2003; Gražulis et al., 2009, 2012, 2015; Merkys et al., 2016, 2023; Quirós et al., 2018; Vaitkus et al., 2021). The results are in good agreement with previous observations by Kobayashi and co-workers, who reported the predominance of amorphous solids for samples aged at up to *T* = 40 °C (Fig. 1, green) and crystalline samples with broad reflections after ageing under at least *T* = 60 °C (Fig. 1, green) (Kobayashi et al., 2019).

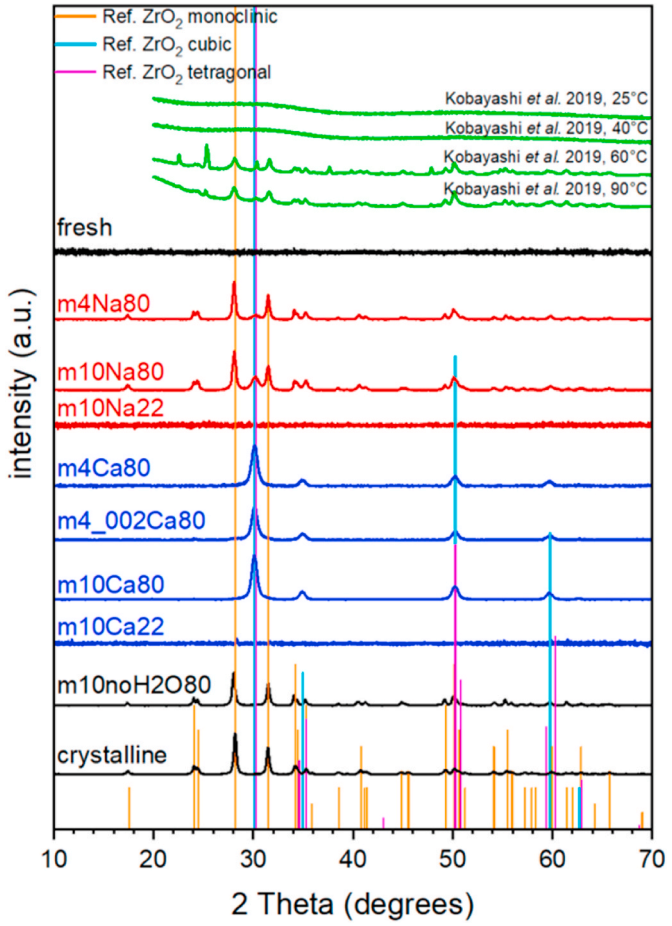

Fig. 1. XRD patterns collected in this work or reported in the literature for the ZrO_2(s) samples: red: solid phases aged in NaOH solutions at T = 22 and 80 °C; blue: solid phases aged in $CaCl_2$–$Ca(OH)_2$ solutions; black: freshly precipitated ZrO_2(am, hyd, fresh) and crystalline ZrO_2(cr) phases; green: diffractograms reported by Kobayashi and co-workers for solid phases aged at T = 25–90 °C (Kobayashi et al., 2019). Vertical lines indicate reference data reported for ZrO_2(cr) in the COD database (Downs and Hall-Wallace, 2003; Gražulis et al., 2009, 2012, 2015; Merkys et al., 2016, 2023; Quirós et al., 2018; Vaitkus et al., 2021): ZrO_2 monoclinic (COD ID: 1528984), ZrO_2 tetragonal (COD ID: 1539831), ZrO_2 cubic (COD ID: 5000038). (For interpretation of the references to colour in this figure legend, the reader is referred to the Web version of this article.)

The XRD powder pattern of crystalline commercial ZrO_2 was refined in the monoclinic $P12_1/c1$ space group using the data of Sirotinkin et al. (2022b). The poor fit at the beginning led to closer check of the model structure in terms of bond distances. An unusual great variation of the Zr–O distances from 1.8 to 2.57 Å was noticed in order to achieve the 7-fold coordination. Therefore, the structure was refined in terms of atomic positions and isotropic thermal parameters (B_{iso}). The data obtained are listed in SI file. The variation of the Zr–O bond lengths is between 2.06 and 2.28 Å with a mean of 2.151 Å (Tables SI–2). The size of the coherent scattering domains is 38(1) nm (Tables SI–1). The resulted structure was further used for consequent Rietveld refinements of our samples.

The refinement of sample m10noH_2O80 showed that the major phase is further monoclinic ZrO_2 (92.2(4) wt%), but also tetragonal polymorph with low crystallinity is present (7.8(4)wt%). The crystallite size of the monoclinic phase is also lower (26 nm) than that of the starting material (38 nm). The results are shown in Figs. SI–3 and Tables SI–3.

To distinguish between the cubic and the tetragonal structure, Rietveld refinements of samples aged in NaOH (m4Na80, m10Na80) were also performed. The main difference between the cubic and tetragonal modifications is the enlargement of one of the crystallographic axes due to distortion of oxygen from the 8c Wyckoff position (¼ ¼ ¼) in the structure of fluorite type. The main difficulties for distinguishing between cubic and tetragonal polymorphs arise from the small atomic scattering factor of oxygen and the great extent of intrinsic disorder (vacancies defects). Due to the broadness caused by apparent very small size of the coherent scattering domains of the cubic phase, a splitting to tetragonal peaks could be fitted in there (110t and 002t under 002c and 200t and 112t under 220c etc.). Although the peak typical for the tetragonal polymorph 102 at 43.3° 2theta is missing, based on the Raman data (see discussion below) we assume presence of tetragonal rather than cubic modification. Therefore, at the beginning of the refinement only monoclinic, $P12_1/c1$, and tetragonal, $P4_2/nmc$ (Sirotinkin et al., 2022a), polymorphs were considered. Quantitative Rietveld analyses of the powder data of samples m4Na80 and m10Na80 resulted in clear presence of monoclinic and tetragonal polymorphs in different proportions. In Table 2 the results of the refinements are listed

Table 2
Results of the Rietveld refinement of samples m4Na80 and m10Na80.

Samples	m4Na80		m10Na80	
phase	*monoclinic* $P12_1/c$	*tetragonal* $P4_2/nmc$	*monoclinic* $P12_1/c$	*tetragonal* $P4_2/nmc$
wt%	82.8(6)	17.2(6)	72.0(7)	28.0(7)
a(Å)	5.159(4)	3.625(4)	5.155(3)	3.628(3)
b(Å)	5.214(4)		5.214(3)	
c(Å)	5.329(4)	5.100(7)	5.325(3)	5.100(4)
β(°)	99.615(4)		99.555(5)	
LVol-IB(nm)	29(2)	6.1(4)	28(2)	6.8(3)
Criteria of fit	Rwp = 6.84 Rexp = 5.41 GOF = 1.27 DWS = 1.23		Rwp = 7.47 Rexp = 5.23 GOF = 1.43 DWS = 1.01	

including quantitative phase information, lattice parameters, size of the coherent scattering domains and criteria of fit. Fig. 2 shows the resulting Rietveld plots for both samples. Sample m10Na80 contains 72.0(7) wt% monoclinic and 28.0(7) wt% tetragonal polymorphs, respectively. In addition, the size of the coherent scattering domains (apparent "crystal size") is 28(2) nm and 6.8(3) nm for the monoclinic and tetragonal polymorph, respectively. In contrast, the sample m4Na80 consists of 82.8(6) wt% monoclinic and 17.2(6) wt% tetragonal polymorphs. The "crystal size" of the tetragonal polymorph is slightly smaller (6.1(4) nm) compared to the m10Na80 sample but the difference is very close to the standard deviation. The monoclinic modification shows no size difference within the estimated standard deviation. The refinement of the unit cell parameters of the tetragonal polymorph results in both cases in a = 3.63 Å and c = 5.100 Å. The unit cell parameters of monoclinic modification are for sample m10Na80 a = 5.155(3) Å, b = 5.214(3) Å, c = 5.325(3) Å, beta = 99.555(5)° and a = 5.159(4) Å, b = 5.214(4) Å, c = 5.329(4) Å, beta = 99.615(4)° for m4Na80, respectively.

In contrast to the crystal structures identified in systems aged in NaOH solutions, the samples aged in presence of Ca (Fig. 1, blue diffractograms) show XRD patterns with main reflections at 2θ = 30.1, 34.9, 50.2 and 59.7°, in agreement with reference patterns reported for cubic (Fig. 1, cyan) and tetragonal (Fig. 1, magenta) ZrO_2(cr) structures. However, a closer look in the 2theta range 20–36° of the m10Ca80 sample reveals not only a large broadening of the flanks of the 111 cubic reflections, but also an increased intensity at about 24° 2theta (Fig. 3). Therefore, not only the cubic structure, but also the monoclinic one was included in the Rietveld refinement. Implementing the pure ZrO_2 cubic structure resulted in some intensity discrepancies between 111 and 200 reflections (lower calculated than observed) on the one side and 220, 311 and 222 reflections on the other. The R-values showed quite high GOF (goodness of fit) (3.49) and DWS (Durbin-Watson statistics) (0.17) values. Including preferred orientation in 111 direction considerably improved the fit. Constrained variation in the occupancy of the Zr position (4a) allowing incorporation of Ca further led to better R-values and plot appearance (see Fig. 4).

The occupancy remained static around values of 30% Ca and 70% Zr ± 3% in the following refinements. Up to this point the isotropic thermal parameters, B_{iso}, were assumed to be 1.0 for all atoms and correspondingly fixed to this value. After fixing the occupancy of Zr and Ca to the values of 0.70 and 0.30, respectively, the B_{iso} were allowed to refine. The best fit (Table 3) was achieved with B_{iso} for Zr and Ca = 2.0, which implies relatively high degree of disorder.

According to Ploc (1981), the observed unit cell parameter a = 5.137 Å would be an indication for incorporation of Ca, but it is not unambiguous. It is difficult to relate the size of a and the degree of substitution of Zr due to mostly two reasons. On the one side, the substitution of Zr is coupled with O vacancies. On the other side, ZrO_2 is prone to defects showing great variation of a between 5.135 Å (ICSD 72955) and 5.1523 Å (ICSD 72956) for non-defect and defect structures, respectively.

Recalling the findings of stoichiometric structures with composition $CaZr_4O_9$ (Rabenau, 1956) and observed presence of monoclinic domains in Ca and Hf stabilized zirconia (Allpress and Rossell, 1975), we introduced the structure described by Marxreiter et al. (1990). The C2/c structure of $CaZr_4O_9$ considers ordering of the calcium ions and O-vacancies along the ⟨110⟩ and ⟨111⟩ directions of the ideal fluorite structure. Refinement resulted in minor quantity of ordered C2/c phase compared to the cubic structure and the result was not improved substantially. Also, the model of defect CaF_2 structure of $Ca_{0.134}$ $Zr_{0.866}$ $O_{1.7}$ proposed by Morinaga and Cohen (Morinaga et al., 1979) which considers defect O positions (additional O position at 0.3, ¼, ¼ was tried, but with moderate success. Refinement of the x position of the defect oxygen returned to ¼ as in the non-defect structure. Therefore, the best result remained the one shown in Table 3. The resulting Rietveld plot is shown in Fig. 2. The stabilization of the cubic polymorph via incorporation of slightly larger ions is widely discussed in the literature available (Pramanik et al., 2018). Also presence of Frenkel defects is considered as possible reason (Tolborg and Walsh, 2023).

Both samples m4Ca80 and m4_002Ca80 show enhanced scattering in their XRD patterns. This suggests presence of the monoclinic modification of $CaZr_4O_9$. Therefore, this phase was included in the refinements. In addition, enhanced presence of amorphous content (about 30 wt%) is observed compared to sample m10Ca80. The results of the Rietveld refinements confirmed prevalence of monoclinic phases (70 wt%) over cubic ZrO_2 (30 wt%) in sample m4_002Ca80. The share of $CaZr_4O_9$

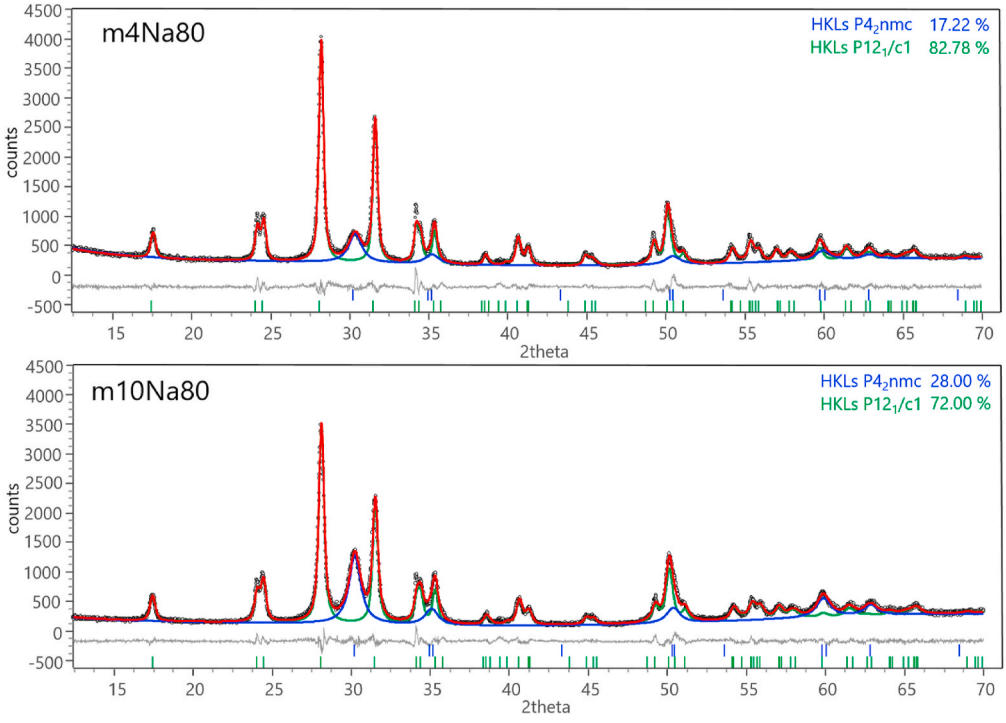

Fig. 2. Rietveld plots of the refinements of samples m4Na80 (top) and m10Na80 (bottom).

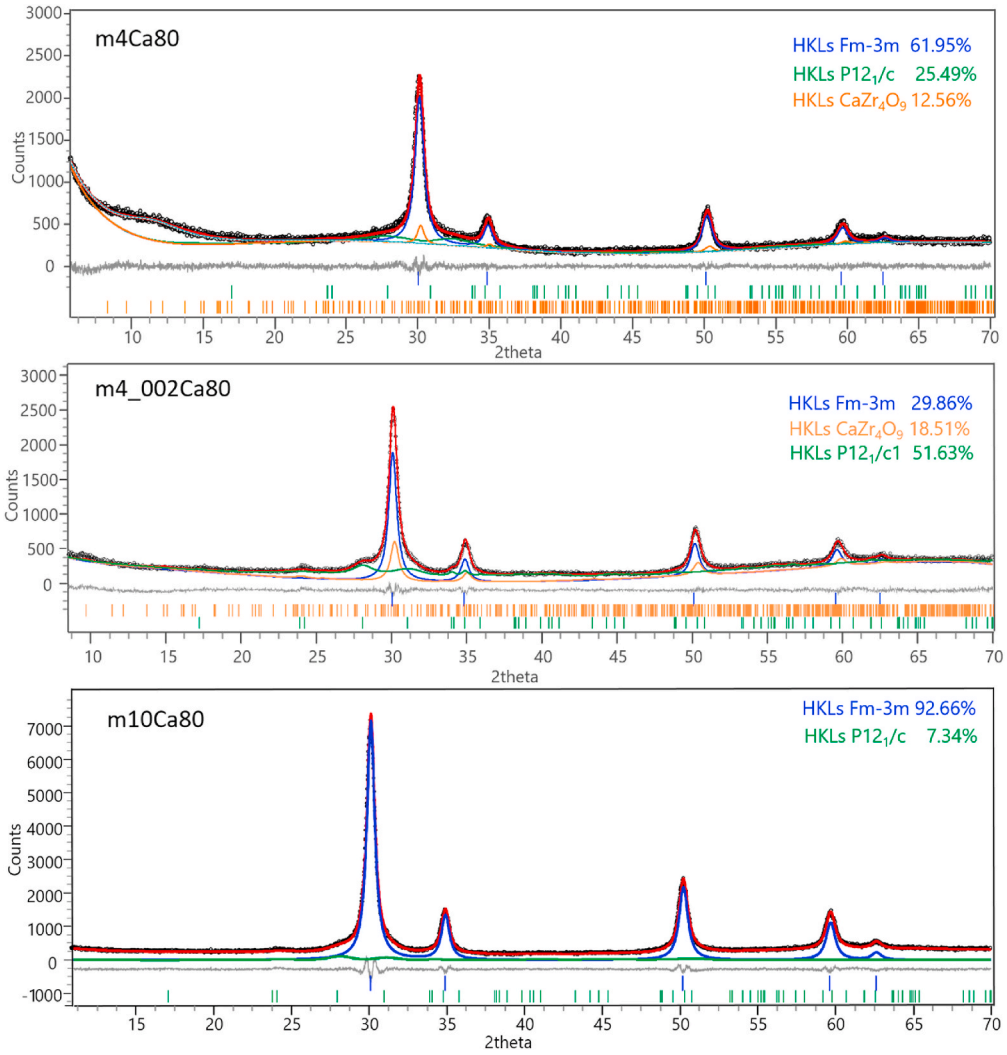

Fig. 3. Rietveld plots of the refinements of samples m4Ca80 (top), m4_002Ca80 (middle) and m10Ca80 (bottom).

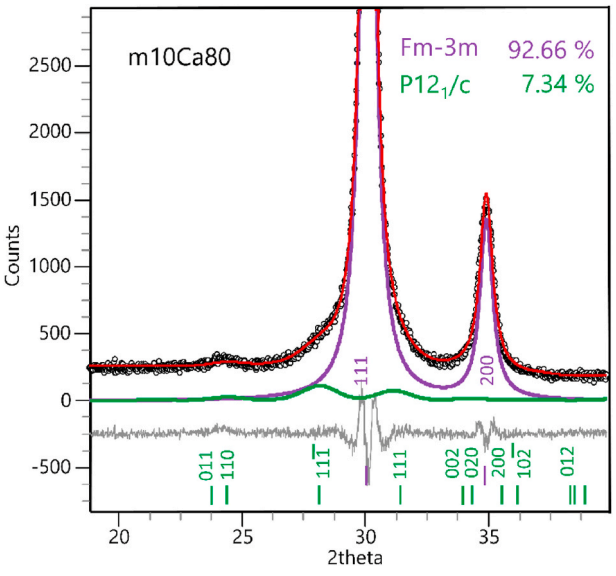

Fig. 4. Rietveld plot of the refinements of sample m10Ca80. 2theta range around reflections 111 and 200 of the cubic modification. Presence of the monoclinic ZrO_2 with corresponding HKL's.

Table 3
Results of the Rietveld refinement of samples m4Ca80, m4_002Ca80 and m10Ca80. Besides a unit cell parameter, occupancies on the Wyckoff positions 4a for Zr and Ca and 8c for O and corresponding temperature factors (B_{iso}) are given for the cubic modification.

Sample	m4Ca80	m4_002Ca80	m10Ca80
space group	*Fm-3m*	*Fm-3m*	*Fm-3m*
wt%	62(4)	30(5)	92.7(6)
a(Å)	5.143(19)	5.144(14)	5.138(5)
cell volume (Å^3)	136.0(15)	136.1(11)	135.7(4)
LVol-IB(nm)	8.2(2)	9.7(2)	10.2(1)
occ Zr (4a 0.0.0)	0.81(1)	0.76(2)	0.70(2)
occ Ca (4a 0.0.0)	0.19(1)	0.24(2)	0.30(2)
occ O (8c ¼.¼.¼)	0.91(1)	0.88(1)	0.85(1)
B_{iso} 4a	2.0	2.0	2.0(2)
B_{iso} 8a	1.5	1.5	1.2(2)
R_{Bragg}	0.245	0.162	0.221
Criteria of fit	Rwp = 5.69	Rwp = 7.48	Rwp = 5.86
	Rexp = 5.09	Rexp = 6.03	Rexp = 4.71
	GOF = 1.12	GOF = 1.24	GOF = 1.25
	DWS = 1.54	DWS = 1.34	DWS = 1.35

comprises 18.5 wt%. The cubic polymorph shows incorporation of 0.24 (2) % Ca on Zr position (Table 3). Sample m4Ca80 is dominated by the cubic polymorph (62 wt%) once again stabilized by Ca. In this case Ca occupies around ¼ of the Zr position.

The size of the crystal domains, determined by Scherrer analysis (Scherrer, 1918), resulted in 23–27 nm for all monoclinic solids and 11–14 nm for all cubic/tetragonal solids. These results are very close to those obtained from the double Voigt approach. Slight tendency for increasing of the domain size from 4 to 10 months ageing time, was observed (Table 3). The size of the crystal domains determined for the commercial ZrO_2(cr) (monoclinic) was as well 27 nm. It is important to note that the crystallization in the cubic/tetragonal structures takes place both in solutions containing 0.2 M Ca as well as in those with 0.02 M Ca. This indicates that even lower Ca concentrations, as expected in cementitious systems (0.02 M as defined by equilibrium with portlandite at pH = 12.5) prevent (i) the crystallization in the form of the monoclinic ZrO_2 structure and (ii) the growth of the ZrO_2 particles to the size achieved in Ca-free systems. Gazzoli and co-workers investigated the incorporation of Ca and Cd in the ZrO_2 structure by means of XRD and Raman spectroscopy (Gazzoli et al., 2007). The Ca-bearing solid phases were prepared by contacting a freshly precipitated ZrO_2(s) with 1 M Ca $(NO_3)_2$ in the pH range 6–12. After shaking the suspensions for 72 h at room temperature, the solid phases were separated from the liquid fraction. After drying at 383 K for 24 h, the samples were subsequently heated in air at 1073 K for 5 h. This synthesis route resulted in tetragonal/cubic ZrO_2(cr), with an excess of $CaZrO_3$ and CaO. In contrast to Gazzoli and co-workers, our results confirm that the equilibration with lower Ca concentrations in the aqueous phase (e.g., 0.02 or 0.2 M) results in the only formation of tetragonal/cubic ZrO_2(cr).

3.1.2. TEM and SEM

TEM images and electron diffraction in Fig. 5 show the presence of different families of particles in the aged solids. For the fresh ZrO_2, TEM shows particles with homogenous shape and size (Fig. 5a). Electron diffraction indicates a rather amorphous character with weak signals fitting to the cubic/tetragonal structure (Figs. SI–4, top). The solid phases aged at $T = 22$ °C in 0.2 M $CaCl_2$ and 0.001 M NaOH show also a dominantly amorphous character, with traces of the cubic/tetragonal structure in the case of ageing in presence of Ca. The solid phases aged at $T = 80$ °C in 0.001 M NaOH (4 and 10 months) show 3 different morphologies, primary particles with a size ≈ 3 nm, particles with a size of ≈ 10 nm and large rods with a length up to 300 nm (Fig. 5b–d). Their electron diffraction shows monoclinic structure with smaller contributions of cubic/tetragonal ZrO_2 (Figs. SI–4, bottom). The solid phases aged at $T = 80$ °C in presence of Ca (4 months, 10 months, 0.2 M $CaCl_2$, 0.02 M $CaCl_2$) show primary particles with a size of 1–3 nm and larger particles with a size of 10–20 nm (Fig. 5f–h). Electron diffraction confirms the cubic/tetragonal structure observed by XRD (see Figs. SI–4, middle). The TEM images of the solid phase aged without liquid phase show aggregates with a size up to 200 nm consisting of smaller particles. The electron diffraction indicates the presence of monoclinic particles and a smaller contribution of a cubic/tetragonal phase. TEM shows also that the commercially obtained crystalline solid consists of homogenous spherical monoclinic particles (Fig. 5e).

SEM images show also different morphologies of the particles, but contain no further information compared to TEM. SEM-EDX measurements summarized in Table 4 confirm the systematic presence of Ca in all solids aged in $CaCl_2$, both at T = 22 and 80 °C. This observation, in connection with the lower presence/absence of chloride, supports that Ca is incorporated into the structure of ZrO_2(s) with Zr:Ca atomic ratios of 3.2–10.3. Table 4 reflects also greater [O]/[Zr] ratios for ZrO_2(am, hyd, fresh), as well as for solid phases aged at T = 22 °C. This observation supports the greater content of OH^-/H_2O in more amorphous samples, as opposed to the lower [O]/[Zr] ratios observed for the more crystalline samples, approaching a ratio of 2. In qualitative terms, solid phases aged at T = 80 °C in NaOH solutions show smaller [O]/[Zr] ratios than those aged at the same temperature in $CaCl_2$–$Ca(OH)_2$ solutions. This correlates well with the larger crystal domains quantified for the former.

3.1.3. Raman spectroscopy

Raman spectroscopy, being sensitive to the polarizability of the ions (inclusive those with small X-ray scattering factors), is often used to overcome the difficulties in distinguishing cubic and tetragonal ZrO_2 polymorphs by XRD. Raman spectra reported for the monoclinic modification of ZrO_2 show presence of many bands including strong lines at 180, 190, 380 and 476 cm^{-1}, bands with moderate intensity at 102, 330 and 345 cm^{-1} as well as low intensity peaks at 220, 305, 500, 537, 555, 614 and 635 cm^{-1} (Bouvier et al., 2001; Garg et al., 2012; Keramidas and White, 1974). The number of the observed bands is close to the expected 18 Raman active vibrational modes of $9A_g$ and $9B_g$ symmetry by factor group analysis (Sekulić et al., 1997). For tetragonal ZrO_2, 6 Raman active bands are predicted, A_{1g}, $2B_{1g}$ and $3E_g$. The spectra published suggest presence of bands at 148 cm^{-1} (E_g) (Bouvier et al., 2001; Keramidas and White, 1974; Štefanić et al., 1998), 263 cm^{-1} (Keramidas and White, 1974), 267 cm^{-1} (Štefanić et al., 1998) - 269 cm^{-1} (Garg

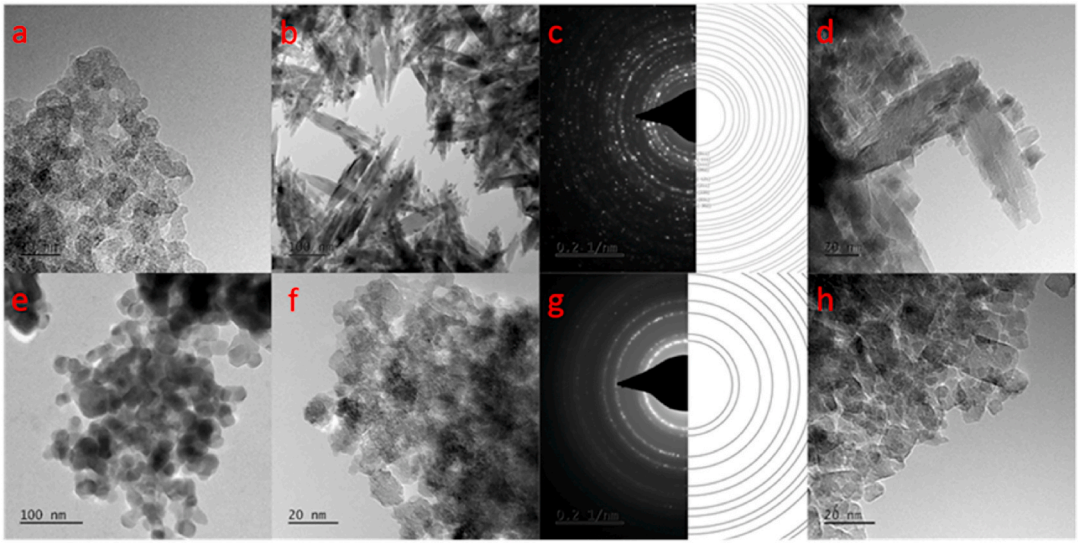

Fig. 5. TEM images and electron diffraction of: (a) fresh, (b, c) m4Na80 (aged for 4 months at T = 80 °C in 0.001 M NaOH), (d) m10Na80 (aged for 10 months at T = 80 °C in 0.001 M NaOH), (e) commercial crystalline, (f, g) m4Ca80 (aged for 4 months at T = 80 °C in 0.2 M $CaCl_2$) and (h) m4_0.02Ca80 (aged for 4 months at T = 80 °C in 0.02 M $CaCl_2$) solid phases.

Table 4
Weight (w%) and atomic (a%) percentages of Zr, O, Ca and Cl for the different solid phases determined by SEM-EDX.

Solid phase	Zr		O		Ca		Cl		[O]/[Zr]	[Zr]/[Ca]
	w%	a%	w%	a%	w%	a%	w%	a%		
fresh	53.0 ± 2.9	16.5 ± 2.7	31.0 ± 0.9	55.0 ± 4.8					3.3 ± 0.8	
m10Ca22	52.5 ± 1.0	16.8 ± 0.3	29.7 ± 0.9	54.2 ± 1.7	5.0 ± 0.3	3.6 ± 0.2	1.4 ± 0.2	1.1 ± 0.2	3.2 ± 0.2	4.7 ± 0.4
m10Na22	58.5 ± 1.2	19.5 ± 0.4	27.6 ± 1.0	52.4 ± 1.8					2.7 ± 0.1	
m4Ca80	49.6 ± 2.4	15.7 ± 2.3	32.8 ± 0.9	59.3 ± 4.8	6.5 ± 0.2	4.7 ± 0.4	1.8 ± 0.2	1.4 ± 0.4	3.8 ± 0.9	3.3 ± 0.9
m4_002Ca80	66.1 ± 1.2	25.4 ± 0.5	22.5 ± 1.0	49.3 ± 2.1	2.9 ± 0.3	2.5 ± 0.3			1.9 ± 0.1	10.2 ± 1.6
m10Ca80	62.5 ± 1.4	22.5 ± 0.5	24.2 ± 1.3	49.7 ± 2.6	3.5 ± 0.4	2.8 ± 0.4			2.2 ± 0.2	8.0 ± 1.6
m4Na80	62.4 ± 2.0	22.7 ± 2.2	28.6 ± 0.6	59.4 ± 3.6					2.6 ± 0.4	
m10Na80	69.7 ± 1.0	27.3 ± 0.4	22.3 ± 0.7	49.8 ± 1.6					1.8 ± 0.1	
m10noH2O80	71.3 ± 1.2	29.2 ± 0.5	23.3 ± 1.0	54.3 ± 2.3					1.9 ± 0.1	
crystalline	72.6 ± 1.4	30.2 ± 0.6	21.2 ± 1.1	50.2 ± 2.6					1.7 ± 0.1	

The total a% and m% are different from each other and different from 100% because carbon from carbon coating of the samples is not shown.

et al., 2012) (A_{1g}), 323 cm^{-1} (B_{1g}), 476 cm^{-1} (Keramidas and White, 1974) - 462 cm^{-1} (Garg et al., 2012; Štefanić et al., 1998) (E_g), 607 cm^{-1} (B_{1g}) and 646 cm^{-1} (E_g) (Garg et al., 2012). The presence of 2 types of tetragonal structures t' and t'' (Yashima et al., 1994) (sometimes referred to as t and t', respectively) makes the interpretation of the Raman spectra more difficult, but there is some dependency of the frequencies of the vibrational modes which allow differentiation between t' and t''. For example, the E_g mode in the range 460–480 cm^{-1} of the t'' shows higher frequency as the t' mode (Sobol and Voronko, 2004; Yashima et al., 1994). Cubic ZrO_2 should give rise to only one Raman active mode due to its fluorite-type structure. However, the single mode (F_{2g}) assigned at 600 cm^{-1} is never observed alone in the spectra of cubic ZrO_2 due to disorder induced contributions from all points of the Brillouin zone to the spectrum (Cai et al., 1995).

Raman spectra of the solid phases under investigation reflect the polymorphism of the ZrO_2 in the samples (Fig. 6) thus being consistent with the XRD results to a large extent. The solids with monoclinic structure, according to XRD and TEM (samples aged in NaOH at 80 °C as well as crystalline ZrO_2 and m10noH$_2$O80), show well defined Raman bands. Sharp bands at 102-106 cm^{-1}, an intense duplet around 178 and 188 cm^{-1}, as well as several peaks between 300 and 380 cm^{-1} including 306, 329, 343 and 380 cm^{-1} are observed. Further, these spectra are characterized by a strong band at 476 cm^{-1} and accompanied by bands with lower intensity at 537, 555, 614 and 636 cm^{-1}. The spectra are in

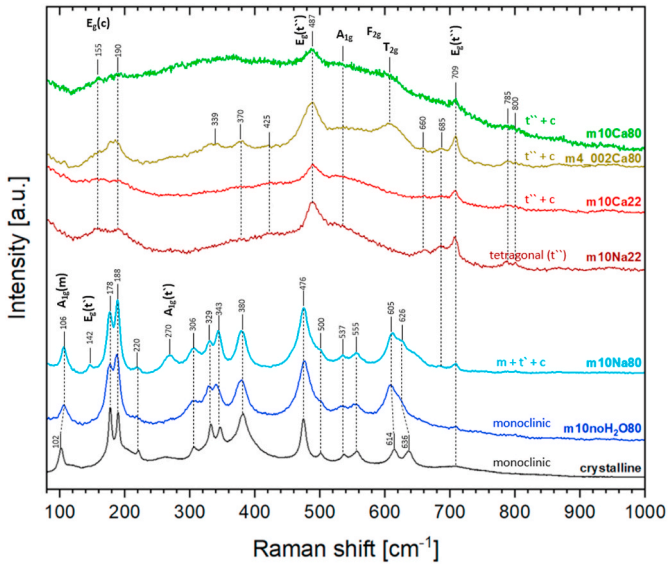

Fig. 6. Raman spectra of the samples in the range 80–1000 cm^{-1}, m - monoclinic, t' - tetragonal, t'' - intermediate tetragonal, c - cubic. The assignments of the modes of the sample m10Ca80 E_g, A_{1g}, T_{2g} stem from the polarization works in (Feinberg and Perry, 1981; Ishigame and Yoshida, 1987).

good agreement with the monoclinic modification. In addition, the spectra of the samples aged in NaOH at 80 °C show bands at 142 and 270 cm^{-1}, which could be assigned to E_g and A_{1g} mode of a tetragonal ZrO_2, respectively. Additionally, these spectra show quite broadened bands in the range 600–650 cm^{-1} with extended shoulders on the high frequency side. These features suggest also presence of cubic ZrO_2. The tetragonal/cubic (XRD, TEM) solids m4_002Ca80 and especially m10Ca80 as well as the X-ray amorphous solids aged at T = 22 °C (m10Ca22 and m10Na22) show generally less defined spectra, which is a hint for disorder mostly due to presence of oxygen vacancies (O_v) in $Zr_{1-x}R_xO_{2-x}(O_v)$ (Yashima et al., 1994). The four samples share some similar features as the broad bands at 155 cm^{-1} and 190 cm^{-1}, intense band at 487 cm^{-1}, relatively sharp band at 709 cm^{-1} as well as ill-resolved humps at about 660, 685 and 785-800 cm^{-1}. The less defined but observable signals of the X-ray amorphous samples aged at T = 22 °C at the same wavenumbers as for tetragonal/cubic solids supports the observation of weak tetragonal/cubic electron diffraction signals by TEM, indicating a possible pre-ordering in these amorphous solids. The main band observed at 487 cm^{-1} could be assigned to E_g in a tetragonal symmetry, though its Raman shift is higher than the reported 462-476 cm^{-1}, pointing to t'' polymorph which is known as an intermediate in the tetragonal–cubic transition (Yashima et al., 1994). The bands observed in the range 650–710 cm^{-1} (also seen as abroad hump in the spectrum of the monoclinic ZrO_2) as well as those at 750-800 cm^{-1} are seldom explained in literature (mostly regarded as defect bands), but are clearly seen in tetragonal and cubic ZrO_2 [(Sekulić et al., 1997), Fig. 2]. All samples aged in $CaCl_2$ at T = 80 °C show in addition a quite broad feature between 500 and 640 cm^{-1}. The increased scattering in this range for the samples m10Na22, m10Ca22, m4_002Ca80 and m10Ca80 suggests an increased "cubicity". The typical bands for the tetragonal polymorph should include strong A_{1g} modes in the range 240–265 cm^{-1} as shown by Sobol and Voronko (2004) which are not seen in the present spectra except some low intensity bands at 270 cm^{-1} in m10Na80. Barberis et al. showed clearly that the most intense band of the tetragonal phase at 267 cm^{-1} (A_{1g}) shifts to lower frequency with increasing cubicity (Barberis et al., 1997) reaching 150 cm^{-1}, which is a typical band for stabilized cubic phase as shown by polarization spectra (Phillippi and Mazdiyasni, 1971). Keramidis and White (Keramidas and White, 1973) studied the Raman scattering of cubic ZrO_2 stabilized with 15% Ca and provide, similarly to Hirata et al. and Sekulic et al. for Y doped cubic samples (Hirata et al., 1994; Sekulić et al., 1997), slightly different Raman spectra as observed for the present samples. On the other hand, the observed spectra agree with the polarized spectra of cubic ZrO_2 provided by (Feinberg and Perry, 1981; Ishigame and Yoshida, 1987).

However, the Raman spectra are greatly influenced by the defect-induced Raman modes (due to oxygen vacancies and displaced O ions), probably manifested by increased intensity of the broad band at 550 cm^{-1} assigned sometimes as A_{1g} of the t'' structure. The band at 600 cm^{-1} observed for m4_002Ca80 can be clearly assigned to T_{2g}

modes in cubic zirconia. Nevertheless, the spectrum of this sample shows also strong bands in the 170-190 cm^{-1} range and 300-400 cm^{-1} range, which are characteristic for the monoclinic phase. Indeed, the XRD data show enhanced quantity of monoclinic $P2_1/c$ phase (51.5 wt %) and $CaZr_4O_9$ monoclinic phase (18.5 wt%).

The investigated solid phases could be summarized and subdivided in 3 groups according to their Raman spectra: 1) purely monoclinic ZrO_2 solid phases (crystalline, m10noH2O80); 2) mainly monoclinic ZrO_2 containing smaller contributions of tetragonal (t') ZrO_2 (solids aged in NaOH at T = 80 °C) and 3) tetragonal (t'') ZrO_2 (solids aged at 22 °C and in $CaCl_2$ at T = 80 °C) with increased cubic character in the row m10Na22 → m10Ca22 → m10Ca80. Some exception represents the sample m4_002Ca80, which shows characteristics of mixed cubic and monoclinic ZrO_2 and monoclinic $CaZr_4O_9$ phases. It is shown that with increased ageing temperature the mainly monoclinic Na samples additionally stabilize the tetragonal polymorphs (t'), whereas the samples with increased ageing temperature in presence of Ca stabilize the cubic polymorphic modification (t'' → c). Thus, Raman spectroscopy provides a valuable information about the influence of Na and Ca as well as the ageing temperature and duration on the stabilization of the different ZrO_2 polymorphs.

3.1.4. SAXS and EXAFS

SAXS measurements performed with a synchrotron radiation source provide information on particle size distribution, but additionally about some surface properties. The observed inflection points (Fig. 7) in the intensity of the scattering vector q suggest the presence of small primary particles with a size of a few nm and larger aggregates of secondary particles. In the case of solids aged at T = 80 °C in NaOH (m10Na80), three inflection points corresponding to 3 families of particles with different particle sizes were observed, as also shown by TEM. In contrast, the solids aged in $CaCl_2$ (m10Ca80), the solid aged without liquid phase (m10noH2O80), the crystalline solid (crystalline) and the amorphous solids (fresh) show only two inflection points corresponding to 2 families of particles as also observed by TEM. The inflection point at q = 0.15 nm^{-1} was not observed in the SAXS profile of the solids aged in $CaCl_2$–$Ca(OH)_2$ (m10Ca80), while it was observed for other solid phases.

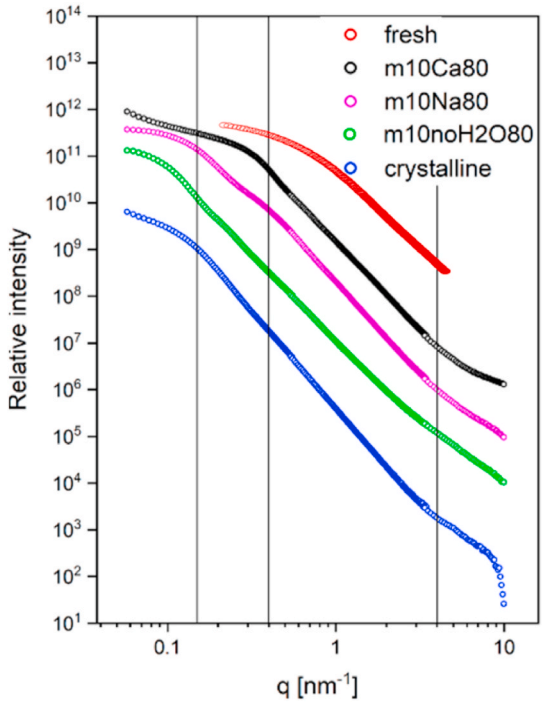

Fig. 7. SAXS measurement of selected ZrO_2 solid phases: fresh, aged at T = 80 °C in NaOH and $CaCl_2$–$Ca(OH)_2$ solutions and commercial crystalline.

Considering that the monoclinic phase is not observed by XRD (Fig. 1) in the solids aged in $CaCl_2$ (m10Ca80), the largest particles corresponding to the inflection at q = 0.15 nm^{-1} observed for the samples m10Na80, m10noH2O80 and "crystalline" are likely to exhibit monoclinic structure. Then, the particle with the size of 10 nm corresponding to q = 0.4 nm^{-1} observed in m10Na80 and m10Ca80 would exhibit tetragonal and/or cubic phase. This behavior is in agreement with previous studies of Pitcher et al. (2005) and Sharma et al. (2018) showing stability crossovers for the different crystal structures depending on particle size/surface area. The slope of the intensity of the scattering vector q in the Porod region (q ≥ 1 nm^{-1}) gives information about the surface roughness of the solids. The slope of 4 after the inflection points at q = 0.15 nm^{-1} observed in the case of the samples aged at T = 80 °C in NaOH and the solid aged without liquid phase and at q = 0.4 nm^{-1} at T = 80 °C in $CaCl_2$–$Ca(OH)_2$ would indicate a smooth surface of monoclinic and tetragonal and/or cubic crystalline particles. In the case of the fresh solid, a slope close to 3 likely corresponds to a rough surface of the aggregates of primary particles observed by TEM. Correlations between crystallinity and surface roughness were previously reported for ceramic thin films and glazes (Hausmann and Gordon, 2003; Mechiakh et al., 2010; Sheikhattar et al., 2016; Trügler et al., 2011). In contrast to the increasing surface smoothness by ageing in the present study, in those studies, crystallization in amorphous thin layers by annealing generally lead to increasing roughness. This behavior, which at first glance appears to be contradictory may be explained by the different crystallization mechanisms. On the one hand, the annealing of amorphous thin layers in these studies leads to rapid and thus to inhomogeneous crystallization, resulting in inhomogeneous and thus rough surfaces. On the other hand, the hydrothermal long-term approach in the present study causes continuous condensation and crystallization processes leading to homogeneous bulk solid phases and with homogeneous and thus smooth surfaces.

The evaluation of the EXAFS spectra with Athena and Artemis software is shown in Fig. 8 and Table 5. Consistent with other techniques, EXAFS analysis of the solids also reflects a different degree of ordering in the investigated ZrO_2 samples. While all samples show a large Zr–O backscattering signal, important differences in the intensity of the Zr–Zr backscattering signals were observed. A weak Zr–Zr backscattering signal is observed for the amorphous samples. Greater amplitudes are observed for the Zr–Zr backscattering of samples aged at T = 80 °C, with the largest Zr–Zr backscattering signal being observed for the ZrO_2 aged without liquid phase and the commercial crystalline solid, thus underpinning the most crystalline character of these samples. These qualitative observations are in line with the fitting approach and the resulting structural parameters. While it was possible to obtain fits of sufficient quality with only one oxygen and one zirconium shell in the case of the amorphous/low crystallinity solid phases (fresh, m10Ca22, m10Na22, m4Ca80), more shells were required to obtain satisfactory fits of the data of the more crystalline samples. For the samples showing a cubic/tetragonal character (m4_002Ca80 and m10Ca80) by XRD/TEM, the addition of a calcium shell improved the fit quality significantly, which is in agreement with the previously shown results suggesting an incorporation of calcium in these samples during the ageing. In this context, several fixed coordination numbers for the calcium shell were evaluated, showing best results for Zr coordinated by 2–3 Ca atoms. In terms of the Zr–O coordination numbers (7.54–8.92) and the distances of the Zr–O shells (2.14–2.16 Å), no significant differences were observed. However, the Zr–Zr coordination numbers (8.88–14.53) and the Zr–Zr distances (3.50–3.55 Å) are higher for the cubic/tetragonal solids compared to the (rather) amorphous samples (4.35–11.74, 3.44–3.47 Å). The higher coordination numbers reflect the higher crystallinity of these samples and the larger distances may be explained by the previously reported increase of the volume of the unit cell (Gazzoli et al., 2007) due to incorporation of Ca in the structure of ZrO_2. This is caused by the differences between the ionic radii of Ca^{2+} and Zr^{4+} ($r_{Ca^{2+}}$ = 1.12 Å and $r_{Zr^{4+}}$ = 0.84 Å; in both cases with coordination numbers (CN) of 8)

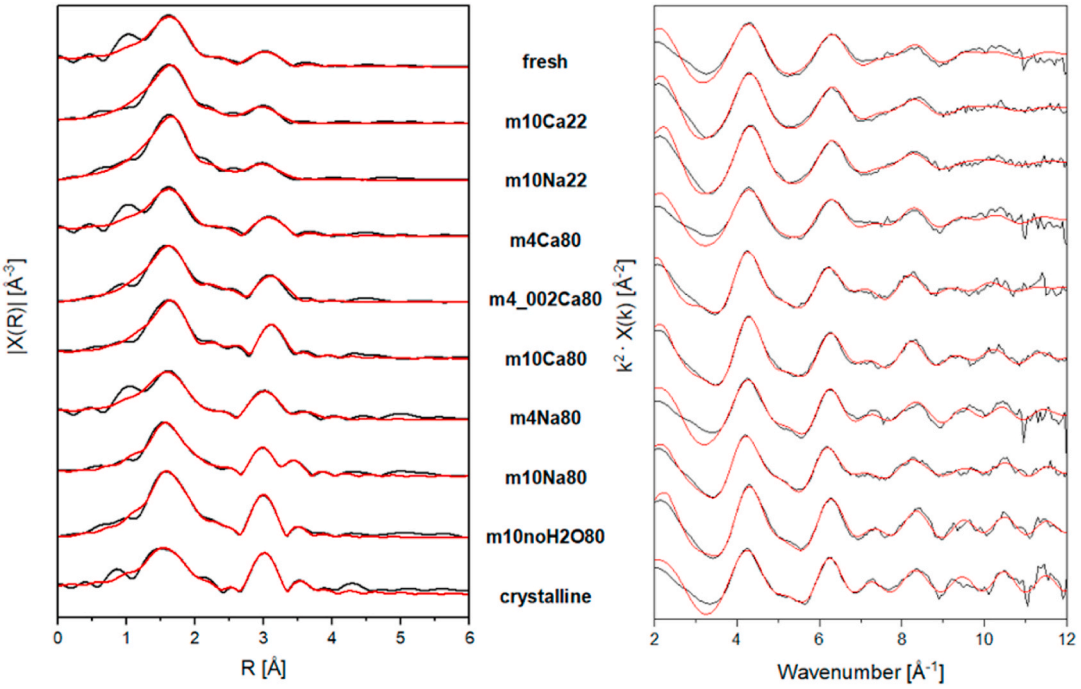

Fig. 8. Fourier transform and EXAFS spectra of the samples in R and k space, respectively. Black and red lines correspond to the measured and fitted spectra, respectively. (For interpretation of the references to colour in this figure legend, the reader is referred to the Web version of this article.)

(Shannon, 1976), and because the incorporation of cations with charge lower than +4 results in anionic vacancies for charge compensation (Gazzoli et al., 2007). For the monoclinic solid phases (m4Na80, m10Na80, m10noH_2O80, crystalline) two or three oxygen and two or three zirconium shells had to be used, partially with coordination numbers fixed to the expected values, to obtain satisfactory fits. This can be explained by the less symmetric monoclinic structure, in which all Zr–O and Zr–Zr distances are different, what is reflected in the fitted Zr–O (2.06–3.69 Å) and Zr–Zr (3.45–4.02 Å) distances. The in total (sum of the shells) higher coordination numbers for Zr–O (10.75–12.85) and Zr–Zr (9.14–13.95) indicate as previously observed the higher crystallinity of these samples.

3.2. Water content and solid composition: TG-DTA, FTIR and XPS

The main quantitative outcome evaluated from the TG-DTA data is the total weight loss measured up to 1200 °C, which is assigned to the number of hydration waters in the investigated hydrous oxides with the assumed stoichiometry $ZrO_2{\cdot}nH_2O$ (Fig. 9). The weight loss and the correlated amount of hydration water of the different solid phases is shown in Table 6. The results in the table clearly show a significantly larger amount of hydration waters in the freshly precipitated solid and the solids aged at $T = 22$ °C (n = 2.0–2.1) compared to the solid phases aged at $T = 80$ °C (n = 0.4 ± 0.2). The sample m4Ca80 represents an exception in the hydration behavior, since this solid phase contains a significant higher amount of water (n = 1.2) compared to other samples aged at $T = 80$ °C and a significant lower amount than the amorphous solids (fresh and aged at T = 22 °C). A possible explanation for this difference could be the presence of an amorphous and a crystalline solid phase in this sample. The hydration behavior of the solid phases is qualitatively confirmed with IR-ATR by comparing the IR intensity in the water region (ca. 2400 cm^{-1} – 3700 cm^{-1}) (see Figs. SI–5 in the Supporting Information). The ratio of H_2O, OH^- and O^{2-} (Table 6) in the ZrO_2(s) solid was determined by fitting the O1s elemental line in the XPS spectra (Fig. 10). As expected, a significantly higher contribution of O^{2-} was observed in the crystalline samples, although no clear differences were observed between solid phases aged in NaOH or $CaCl_2$–$Ca(OH)_2$ systems.

Solid phase characterization by TG-DTA, XPS and IR-ATR evidences that ageing at elevated temperatures strongly impacts the degree of hydration of the solid phases. The transformation from amorphous to crystalline solids occurring at $T = 80$ °C is connected with a reduction of water content and a decreasing [O]/[Zr] ratio. XPS analysis shows that the solids' stoichiometry is described more accurately as $ZrO_x(OH)_{4-2x}{\cdot}nH_2O$ and that the transformation process leads to an increase of O^{2-} contribution and a decrease of H_2O and OH^- contributions. This can be attributed to condensation reactions at the surface of the solids, where two Zr–OH groups release one water molecule to form a Zr–*O*–Zr bond. This behavior is also in agreement with the increasing crystallinity and particle size observed with XRD and TEM.

3.3. Surface properties: BET and ζ-potential

Due to limited amount of material, not all solid phases could be characterized by BET. X-ray amorphous solid phases showed high specific surface areas of 257 m^2g^{-1} (m10Ca22) and 390 m^2g^{-1} (m10Na22), which are in agreement with the small particle size observed with TEM. The value of 199.5 m^2g^{-1} determined for the m4Ca80 solid phase (aged in 0.2 M $CaCl_2$ at 80 °C for 4 months) does not correlate well with the particle size determined by Scherrer analysis of the XRD result of this sample, which suggests a value of 100 ± 20 m^2g^{-1} (uncertainty based on uncertainty of particle size) based on geometric calculations (assumption of spherical particles of homogeneous size) and densities. Such discrepancy could be explained by surface properties, e.g. surface roughness or by the presence of smaller amorphous particles that are not observable with XRD. The latter hypothesis is supported by the identification of smaller particles with TEM and SAXS and would also agree with the higher water content determined for this sample with TG-DTA. Summarizing these observations, the sample m4Ca80 represents an exception since this solid phase shows properties, which indicate the presence of an amorphous and a crystalline phase and thus an incomplete transformation process. This slower kinetics compared to the other 4 months samples could potentially be explained by a slight decrease of the pH of this sample during the ageing, since the transformation

Table 5
Structural data for ZrO_2(s) solid phases obtained by EXAFS fit.

Solid phase	Path	N	R (Å)	σ^2	ΔE_0	Rf
fresh	Zr–O	7.54	2.16	0.009	−3.70	0.009
	Zr–Zr	4.35	3.44	0.013		
m10Ca22	Zr–O	8.74	2.16	0.011	−3.25	0.019
	Zr–Zr	10.60	3.45	0.020		
m10Na22	Zr–O	8.92	2.16	0.010	−2.02	0.018
	Zr–Zr	11.74	3.47	0.022		
m4Ca80	Zr–O	7.20	2.15	0.009	−3.68	0.026
	Zr–Zr	4.64	3.47	0.011		
m4_0.02Ca80	Zr–O	7.73	2.14	0.010	−5.28	0.021
	Zr–Zr	14.53	3.52	0.016		
	Zr–Ca	3.00[a]	3.56	0.013		
m10Ca80	Zr–O	7.72	2.15	0.009	−3.11	0.015
	Zr–Zr	9.67	3.55	0.011		
	Zr–Ca	2.50[a]	3.62	0.002		
m4Na80	Zr–O1	8.85	2.15	0.012	−4.88	0.010
	Zr–O2	4.00[b]	3.64	0.013		
	Zr–Zr1	6.33	3.45	0.010		
	Zr–Zr2	4.00[b]	4.02	0.012		
m10Na80	Zr–O1	2.25	2.07	0.000	−2.94	0.010
	Zr–O2	4.50	2.21	0.005		
	Zr–O3	4.00[b]	3.69	0.016		
	Zr–Zr1	8.03	3.48	0.009		
	Zr–Zr2	4.90	3.63	0.007		
m10noH$_2$O80	Zr–O1	3.90[c]	2.09	0.002	−1.42	0.007
	Zr–O2	3.90[c]	2.23	0.002		
	Zr–O3	4.00[b]	3.63	0.026		
	Zr–Zr1	9.62	3.47	0.008		
	Zr–Zr2	4.33	3.66	0.007		
crystalline	Zr–O1	2.00[b]	2.06	0.002	−3.22	0.012
	Zr–O2	5.89	2.21	0.008		
	Zr–O3	4.00[b]	3.61	0.005		
	Zr–Zr1	4.14	3.46	0.005		
	Zr–Zr2	1.00[b]	3.65	0.001		
	Zr–Zr3	4.00[b]	4.00	0.015		

Coordination numbers (N), bond distances (R (Å)), Debye-Waller factors (σ^2), shift in energy from calculated Fermi level (ΔE_0) and 'goodness of fit' factor (R).
[a] Fixed N with best results selected.
[b] N fixed to expected value.
[c] N(Zr–O1) forced to be equal to N(Zr–O2) as expected for tetragonal structure.

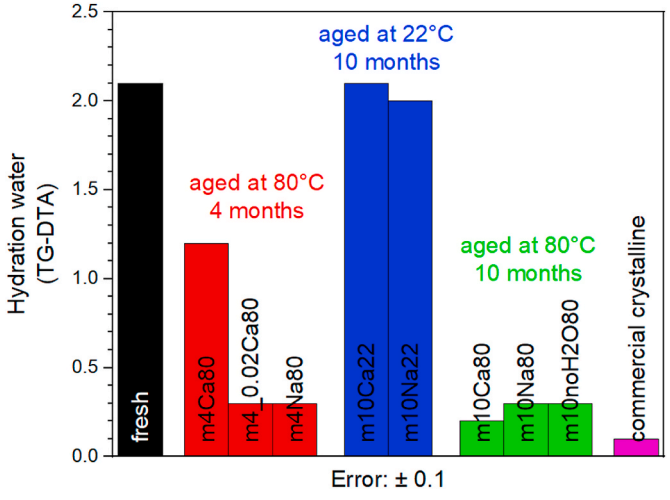

Fig. 9. Number of hydration waters quantified by TG-DTA, calculated based on the weight loss and assuming a stoichiometry of $ZrO_2{\cdot}nH_2O$.

kinetics becomes slower the closer to neutral conditions the pH becomes (Štefanić et al., 1997). The lower values of 36.5 m^2g^{-1} for the m10noH$_2$O80 solid phase (aged dry at 80 °C for 10 months) and 24 m^2g^{-1} for the commercial crystalline solid are also reflected by their larger particle size. BET measurements accordingly support a decrease

Table 6
TG-DTA and XPS results of the Zr(IV) hydrous oxides. Uncertainty of the XPS data ±10%.

Solid	Weight loss (%) TG-DTA	Hydration water TG-DTA	[O]/[Zr] XPS	O^{2-} (mol %) XPS	OH^- (mol %) XPS	H_2O (mol %) XPS
fresh	23.6 ± 0.5	2.1 ± 0.1	3.2	58	42	
m10Ca22	23.7 ± 0.5	2.1 ± 0.1	3.3	52	41	7
m10Na22	22.9 ± 0.5	2.0 ± 0.1	3.1	56	37	7
m4Ca80	15.2 ± 0.5	1.2 ± 0.1	2.9	67	33	
m4_0.02Ca80	4.9 ± 0.5	0.3 ± 0.1	2.6	79	19	3
m10Ca80	2.7 ± 0.5	0.2 ± 0.1	2.7	78	19	3
m4Na80	4.7 ± 0.5	0.3 ± 0.1	2.5	73	27	
m10Na80	4.3 ± 0.5	0.3 ± 0.1	2.5	75	20	5
m10noH2O80	4.3 ± 0.5	0.3 ± 0.1	2.5	71	21	8
crystalline	1.3 ± 0.5	0.1 ± 0.1	2.5	83	13	4

of the surface with ageing, which is in line with the expected Ostwald ripening of amorphous phases and further confirms the observations achieved in this work with a variety of characterization methods.

Zeta potential measurements in 1 mM HCl–NaCl–NaOH systems confirm that the point of zero charge of most investigated solids lays in slightly acidic conditions (pH 5–6), in agreement with the majority of literature data (Figs. SI–6 in the Supporting Information) (Kosmulski, 2009). The samples aged in $CaCl_2$ show less negative zeta potential values in the alkaline region compared to the other solids (Figs. SI–7 in the Supporting Information), whereas measurements conducted in 20 mM $CaCl_2$ show no negative zeta potentials and no points of zero charge.

Considering the pH of the corresponding ageing solutions, measurements of the zeta potential support that the surface of the ZrO_2 solids is negatively charged during the ageing in NaOH but positively charged or near-neutral in $CaCl_2$–$Ca(OH)_2$ solutions due to the presence of surficial Ca^{2+} ions. Even though the incorporation of Ca has been shown to trigger the stabilization of a different crystal structure in ZrO_2 (see Section 3.1), differences in the surface charge can affect the stability and growth of the ZrO_2 particles, e.g., due to charge repulsion of particles aged in a given background electrolyte.

4. Summary and conclusions

The transformation of amorphous ZrO_2(am, hyd) to crystalline phases in aqueous systems was investigated at different temperatures (T = 22 and 80 °C), background electrolytes (NaOH, $CaCl_2$–$Ca(OH)_2$) and contact times (t = 4 and 10 months) using a multi-method approach for the characterization of the solid phases.

XRD, TEM, electron diffraction, SAXS, EXAFS and SEM-EDX confirm that ageing at T = 80 °C induces a transformation from a freshly precipitated amorphous solid towards nano-crystalline solids, with the consequent increase in the particle size. As mechanism for these transformations, the already from literature (Štefanić et al., 1997, 2005) known hydrothermal crystallization by dissolution/precipitation mechanisms is proposed. In agreement with these observations, the solid phase characterization by TG-DTA, XPS and IR-ATR evidences that ageing at elevated temperatures also strongly impacts the degree of hydration of the solid phases. The transformation from amorphous to crystalline solids occurring at T = 80 °C is connected with a reduction of water content and a decreasing [O]/[Zr] ratio. XPS analysis shows that the solids are described more accurately as $ZrO_x(OH)_{4-2x}{\cdot}nH_2O$ and that the transformation process leads to an increase of O^{2-} contribution and a decrease of H_2O and OH^- contributions. In contrast to ageing at T = 80 °C, no changes in the solid properties were observed for solid phases equilibrated at T = 22 °C. For the solid phases aged at T = 80 °C, the ageing time (4 or 10 months) triggers no further evident changes on the

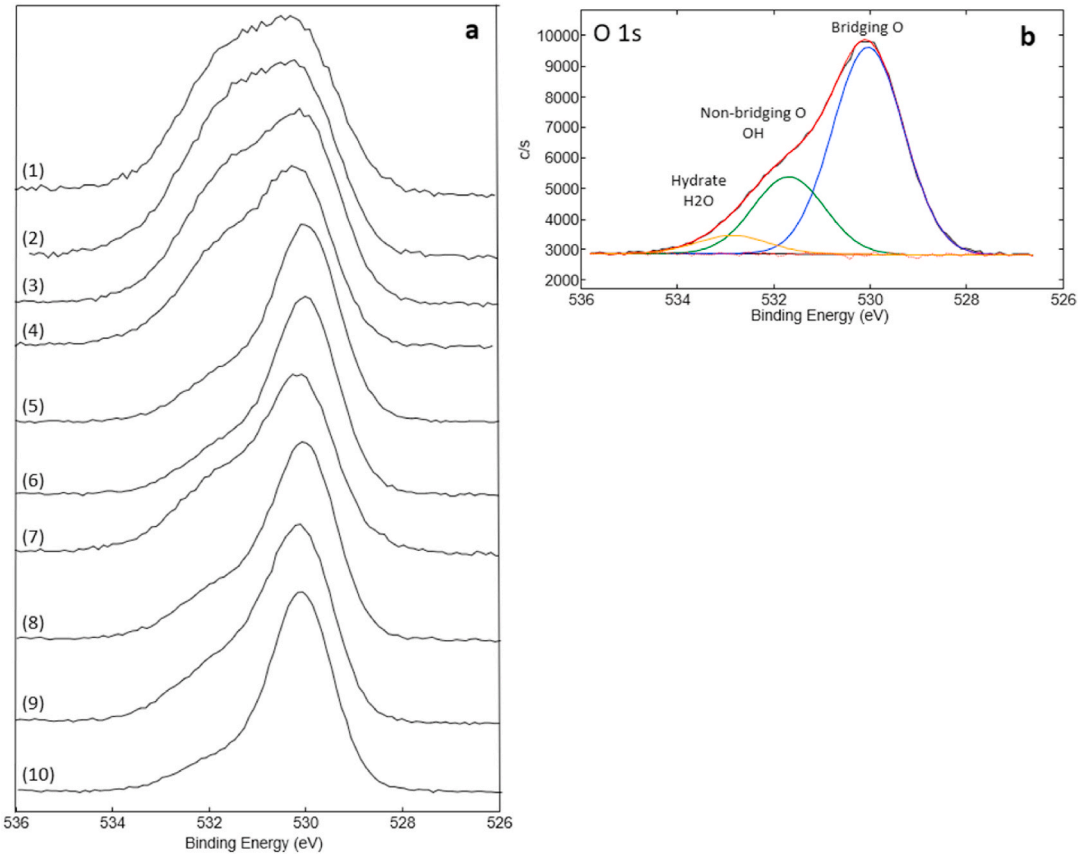

Fig. 10. (a) XPS narrow scans of the O1s elemental line of ZrO_2 solids: (1) fresh, (2) m10Ca22, (3) m10Na22, (4) m4Ca80, (5) m4_002Ca80, (6) m10Ca80, (7) m4Na80, (8) m10Na80, (9) m10noH2O80, (10) commercial crystalline; (b) Example of the fitting of the O1s elemental line.

structure of the solids, indicating that a stabilization takes place already at 4 months (except the sample m4Ca80 as explained in Chapter 3.3).

In contrast to the ageing time, changes in the background electrolyte promote significant alterations in the solid structure. The thermodynamically most stable monoclinic structure is favored in NaOH systems, whereas cubic/tetragonal ZrO_2 is stabilized in Ca systems, even at relatively low background electrolyte concentrations (0.02 M $CaCl_2$), as those expected in cementitious systems. Rietveld analysis of the XRD data, EXAFS and SEM-EDX measurements support that the stabilization of the cubic/tetragonal structure in $CaCl_2$–$Ca(OH)_2$ solutions is caused by the incorporation of Ca in the ZrO_2 matrix, as extensively reported in the literature for Y-doped ZrO_2. The XRD and Raman analysis are also consistent with those reported for $CaZr_4O_9$ solid phases (Pathak et al., 2016; Yeryukov et al., 2014), thus hinting towards the possible formation of mixed Ca–Zr-oxides.

Measurements of the zeta potential of selected solid phases in NaOH and $CaCl_2$–$Ca(OH)_2$ systems show clear differences in the alkaline conditions investigated in this work, with the predominance of negatively charged surfaces in Na-systems and positively-charged surfaces in Ca-systems containing 20 mM $CaCl_2$. Such differences expectedly impact the growth process, and thus may partially explain the different particles sizes observed in both background electrolytes.

This study provides new insights for the understanding of the hydrothermal transformation of ZrO_2(am, hyd) into the thermodynamically stable anhydrous crystalline oxide, ZrO_2(cr). It is shown that transformation processes leading to more crystalline phases into crystal lattices, are complex and the result of reaction time, an interplay of temperature and the incorporation of foreign cations into crystal lattices.

The importance of these transformations lays within the expected difference in solubility of the different solid phases. While crystalline ZrO_2 solid phases are characterized by very low solubilities, the presence of an amorphous phase is expected to enhance the solubility and thus mobility of Zr by several orders of magnitude (Brown et al., 2005).

Furthermore, the study shows that even the low Ca concentrations, which are expected for some repository concepts including cementitious systems, enable the stabilization of a different crystal structure or even the formation of mixed oxides during the hydrothermal crystallization process. The impact of the incorporated Ca ions on the overall solubility of ZrO_2 remains unclear and deserves attention in future experimental studies.

Similar processes may also be of relevance for other M(IV) solid phases of relevance in the context of nuclear waste disposal, e.g., UO_2(am, hyd), PuO_2(am, hyd) or TcO_2(am, hyd).

CRediT authorship contribution statement

Christian Kiefer: Writing – review & editing, Writing – original draft, Visualization, Methodology, Investigation, Formal analysis, Data curation, Conceptualization. **Xavier Gaona:** Writing – review & editing, Validation, Supervision, Project administration, Methodology, Conceptualization. **Tomo Suzuki-Muresan:** Writing – review & editing, Validation, Supervision, Project administration, Methodology, Conceptualization. **Dieter Schild:** Writing – review & editing, Investigation, Data curation. **Krassimir Garbev:** Writing – review & editing, Writing – original draft, Investigation, Data curation. **Taishi Kobayashi:** Writing – review & editing, Investigation, Data curation. **Kathy Dardenne:** Writing – review & editing, Investigation, Data curation. **Oliver Dieste Blanco:** Investigation, Data curation. **Marcus Altmaier:** Writing – review & editing, Validation, Conceptualization. **Bernd Grambow:** Writing – review & editing, Validation, Supervision, Project administration, Methodology, Conceptualization. **Horst Geckeis:**

Writing – review & editing, Validation, Supervision, Project administration, Methodology, Conceptualization.

Declaration of competing interest

The authors declare that they have no known competing financial interests or personal relationships that could have appeared to influence the work reported in this paper.

Acknowledgements

We acknowledge the KIT light source for provision of instruments at their beamlines and we would like to thank the Institute for Beam Physics and Technology (IBPT) for the operation of the storage ring, the Karlsruhe Research Accelerator (KARA).

Appendix A. Supplementary data

Supplementary data to this article can be found online at https://doi.org/10.1016/j.apgeochem.2025.106302.

Data availability

Data will be made available on request.

References

Allpress, J.G., Rossell, H.J., 1975. A microdomain description of defective fluorite-type phases $Ca_xM_{1-x}O_{2-x}$(M = Zr, Hf; x = 0.1-0.2). J. Solid State Chem. 15, 68–78.
Altmaier, M., Gaona, X., Fanghänel, T., 2013. Recent advances in aqueous actinide chemistry and thermodynamics. Chem. Rev. 113, 901–943.
Altmaier, M., Metz, V., Neck, V., Müller, R., Fanghänel, T., 2003. Solid-liquid equilibria of $Mg(OH)_2$(cr) and $Mg_2(OH)_3Cl \bullet 4H_2O$(cr) in the system Mg-Na-H-OH-O-Cl-H_2O at 25 °C. Geochem. Cosmochim. Acta 67, 3595–3601.
Altmaier, M., Neck, V., Fanghänel, T., 2008. Solubility of Zr(IV), Th(IV) and Pu(IV) hydrous oxides in $CaCl_2$ solutions and the formation of ternary Ca-M(IV)-OH complexes. Radiochim. Acta 96, 541–550.
Barberis, P., Merle-Méjean, T., Quintard, P., 1997. On Raman spectroscopy of zirconium oxide films. J. Nucl. Mater. 246, 232–243.
Bouvier, P., Djurado, E., Ritter, C., Dianoux, A.J., Lucazeau, G., 2001. Low temperature phase transformation of nanocrystalline tetragonal ZrO_2 by neutron and Raman scattering studies. Int. J. Inorg. Mater. 3, 647–654.
Brown, P.L., Curti, E., Grambow, B., Ekberg, C., 2005. Chemical thermodynamics of zirconium. In: Chemical Thermodynamics, ume 8. OECD Publishing, Paris.
Bube, C., Metz, V., Bohnert, E., Garbev, K., Schild, D., Kienzler, B., 2013. Long-term cement corrosion in chloride-rich solutions relevant to radioactive waste disposal in rock salt – leaching experiments and thermodynamic simulations. Phys. Chem. Earth 64, 87–94.
Cai, J., Raptis, C., Raptis, Y.S., Anastassakis, E., 1995. Temperature dependence of Raman scattering in stabilized cubic zirconia. Phys. Rev. B 51.
Cevirim-Papaioannou, N., 2018. Redox Chemistry, Solubility and Hydrolysis of Uranium in Dilute to Concentrated Salt Systems (PhD). Karlsruhe.
Craeye, B., De Schutter, G., Van Humbeeck, H., Van Cotthem, A., 2009. Early age behaviour of concrete supercontainers for radioactive waste disposal. Nucl. Eng. Des. 239, 23–35.
Dell'Agli, G., Mascolo, G., 2000. Low temperature hydrothermal synthesis of ZrO_2-CaO solid solutions. J. Mater. Sci. 35, 661–665.
Downs, R.T., Hall-Wallace, M., 2003. The American mineralogist crystal structure database. Am. Mineral. 88, 247–250.
Fábregas, I.O., Lamas, D.G., Acuña, L.M., Walsöe de Reca, N.E., Craievech, A.F., Fantini, M.C.A., Prado, R.J., 2008. Crystal structure and local order of nanocrystalline zirconia-based solid solutions. Powder Diffraction Suppl 23, 46–55.
Feinberg, A., Perry, C.H., 1981. Structural disorder and phase transitions in ZrO_2-Y_2O_3 system. J. Phys. Chem. Solid. 42, 513–518.
Garg, N., Mittal, V.K., Bera, S., Dasgupta, A., Sankaralingam, V., 2012. Preparation and characterization of tetragonal dominant nanocrystalline ZrO_2 obtained via direct precipitation. Ceram. Int. 38, 2507–2512.
Gazzoli, D., Mattei, G., Vagili, M., 2007. Raman and X-ray investigations of the incorporation of Ca^{2+} and Cd^{2+} in the ZrO_2 structure. J. Raman Spectrosc. 38, 824–831.
Gražulis, S., Chateigner, D., Downs, R.T., Yokochi, A.F.T., Quirós, M., Lutterotti, L., Manakova, E., Butkus, J., Moeck, P., Le Bail, A., 2009. Crystallography open database – an open-access collection of crystal structures. J. Appl. Crystallogr. 42, 726–729.
Gražulis, S., Daškevič, A., Merkys, A., Chateigner, D., Lutterotti, L., Quirós, M., Serebryanaya, N.R., Moeck, P., Downs, R.T., Le Bail, A., 2012. Crystallography open database (COD): an open-access collection of crystal structures and platform for world-wide collaboration. Nucleic Acids Res. 40.
Gražulis, S., Merkys, A., Vaitkus, A., Okulič-Kazarinas, M., 2015. Computing stoichiometric molecular composition from crystal structures. J. Appl. Crystallogr. 48, 85–91.
Grenthe, I., Gaona, X., Plyasunov, A.V., Rao, L., Runde, W.H., Grambow, B., Konings, R.J. M., Smith, A.L., Moore, E.E., 2020. Second update on the chemical thermodynamics of uranium, neptunium, plutonium, americium and technetium. In: Chemical Thermodynamics, ume 14. OECD Publishing, Paris.
Hausmann, D.M., Gordon, R.G., 2003. Surface morphology and crystallinity control in the atomic layer deposition (ALD) of hafnium and zirconium oxide thin films. J. Cryst. Growth 249, 251–261.
Hirata, T., Asari, E., Kitajima, M., 1994. Infrared and Raman spectroscopic studies of ZrO_2 polymorphs doped with Y_2O_3 or CeO_2. J. Solid State Chem. 110, 201–207.
Ishigame, M., Yoshida, E., 1987. Study of the defect-induced Raman spectra in cubic zirconia. Solid State Ionics 23, 211–218.
Keramidas, V.G., White, W.B., 1974. Raman scattering study of the crystallization and phase transformations of ZrO_2. J. Am. Ceram. Soc. 57, 22–24.
Keramidas, V.G., White, W.B., 1973. Raman scattering from $Ca_xZr_{1-x}O_{2-x}$, a system with massive point defects. J. Phys. Chem. Solid. 34, 1873–1878. https://doi.org/10.1016/S0022-3697(73)80108-8.
Kiefer, C., Neill, T., Cevirim-Papaioannou, N., Schild, D., Gaona, X., Vitova, T., Dardenne, K., Rothe, J., Altmaier, M., Geckeis, H., 2022. Interlink between solubility, structure, surface and thermodynamics in the ThO_2(s, hyd)–H_2O(l) system. Front. Chem. 10, 1042709.
Kobayashi, T., Bach, D., Altmaier, M., Sasaki, T., Moriyama, H., 2013. Effect of temperature on the solubility and solid phase stability of zirconium hydroxide. Radiochim. Acta 101, 645–651.
Kobayashi, T., Nakajima, S., Motokawa, R., Matsumura, D., Saito, T., Sasaki, T., 2019. Structural approach to understanding the solubility of metal hydroxides. Langmuir 35, 7995–8006.
Kobayashi, T., Sasaki, T., Takagi, I., Moriyama, H., 2016a. Effect of solid phase transformation on the solubility product of thorium hydrous oxide at 363 K. J. Nucl. Sci. Technol. 53, 1787–1793.
Kobayashi, T., Uemura, T., Sasaki, T., Takagi, I., Moriyama, H., 2016b. The solubilities and solubility products of zirconium hydroxide and oxide after aging at 278, 313, and 333 K. Radiochim. Acta 104, 183–193.
Kosmulski, M., 2009. Surface Charging and Points of Zero Charge, first ed. CRC Press, Boca Raton.
Lábár, J.L., 2008. Electron diffraction based analysis of phase fractions and texture in nanocrystalline thin films, Part I: principles. Microsc. Microanal. 14, 287–295.
Li, P., Chen, I.-W., Penner-Hahn, J.E., 1994a. Effect of dopants on zirconia stabilization-an X-ray absorption study: I, trivalent dopants. J. Am. Ceram. Soc. 77, 118–128.
Li, P., Chen, I.-W., Penner-Hahn, J.E., 1994b. Effect of dopants on zirconia stabilization-an X-ray absorption study: II, tetravalent dopants. J. Am. Ceram. Soc. 77, 1281–1288.
Li, P., Chen, I.-W., Penner-Hahn, J.E., 1993a. X-Ray-Absorption studies of zirconia polymorphs. I. Characteristic local structures. Phys. Rev. B 48, 10063–10073.
Li, P., Chen, I.-W., Penner-Hahn, J.E., 1993b. X-Ray-Absorption studies of zirconia polymorphs. II. Effect of Y_20_3 dopant on ZrO_2 structure. Phys. Rev. B 48, 10074–10081.
Li, Z., Lee, W.E., Zhang, S., 2007. Low-temperature synthesis of $CaZrO_3$ powder from molten salts. J. Am. Ceram. Soc. 90, 364–368.
Macklin, R.L., 1985. Neutron capture measurements on radioactive ^{93}Zr. Astrophys. Space Sci. 115, 71–83.
Marxreiter, H., Boysen, H., Frey, F., Schulz, H., Vogt, T., 1990. The structure of the Φ_1-phase $CaZr_4O_9$ in calcium stabilized zirconia. Mater. Res. Bull. 25, 435–442.
Mechiakh, R., Ben Sedrine, N., Chtourou, R., Bensaha, R., 2010. Correlation between microstructure and optical properties of nano-crystalline TiO_2 thin films prepared by sol–gel dip coating. Appl. Surf. Sci. 257, 670–676.
Merkys, A., Vaitkus, A., Butkus, J., Okulič-Kazarinas, M., Kairys, V., Gražulis, S., 2016. COD::CIF::Parser: an error-correcting CIF parser for the perl language. J. Appl. Crystallogr. 49, 292–301.
Merkys, A., Vaitkus, A., Grybauskas, A., Konovalovas, A., Quirós, M., Gražulis, S., 2023. Graph isomorphism-based algorithm for cross-checking chemical and crystallographic descriptions. J. Cheminf. 15.
Metz, V., Geckeis, H., González-Robles, E., Loida, A., Bube, C., Kienzler, B., 2012. Radionuclide behaviour in the near-field of a geological repository for spent nuclear fuel. Radiochim. Acta 100, 699–713.
Morinaga, M., Cohen, J.B., Faber, Jr.J., 1979. X-Ray diffraction study of $Zr(Ca,Y)O_{2-x}$. I. The average structure. Acta Crystallogr. A35, 789–795.
Nishikawa, S., Kobayashi, T., Sasaki, T., Takagi, I., 2018. Solubilities and solubility products of thorium hydroxide under moderate temperature conditions. Radiochim. Acta 106, 655–667.
Northwood, D.O., 1985. The development and applications of zirconium alloys. Mater. Des. 6, 58–70.
Opitz, L., Hübner, R., Shams Aldin Azzam, S., Gilson, S.E., Finkeldei, S.C., Huittinen, N., 2023. Investigations towards incorporation of Eu^{3+} and Cm^{3+} during ZrO_2 crystallization in aqueous solution. Sci. Rep. 13.
Pathak, M.S., Seshadri, M., Singh, N., Singh, V., Lee, J.-K., 2016. Luminescence behaviors and infrared-to-visible energy conversion inEr^{3+}/Yb^{3+} -doped $CaZr_4O_9$ phosphors. Opt. Mater. 62, 717–722.
Phillippi, C.M., Mazdiyasni, K.S., 1971. Infrared and Raman spectra of zirconia polymorphs. J. Am. Ceram. Soc. 54, 254–258.
Pitcher, M.W., Ushakov, S.V., Navrotsky, A., Woodfield, B.F., Li, G., Boerio-Goates, J., Tissue, B.M., 2005. Energy crossovers in nanocrystalline zirconia. J. Am. Ceram. Soc. 88, 160–167.

Ploc, R.A., 1981. The lattice parameter of cubic ZrO_2 formed on zirconium. J. Nucl. Mater. 99, 124–128.
Pramanik, P., Singh, S., Joshi, D.C., Mallick, A., Pisane, K., Romero, A.H., Thota, S., Seehra, M.S., 2018. Cubic phase stability, optical and magnetic properties of Cu-stabilized zirconia nanocrystals. J. Phys. D Appl. Phys. 51.
Quirós, M., Gražulis, S., Girdzijauskaitė, S., Merkys, A., Vaitkus, A., 2018. Using SMILES strings for the description of chemical connectivity in the Crystallography open database. J. Cheminf. 10.
Rabenau, A., 1956. Perowskit- und Fluoritphasen in den Systemen ZrO_2-$LaO_{1,5}$-MgO und ZrO_2-$LaO_{1,5}$-CaO. Z. Anorg. Allg. Chem. 288, 221–234.
Rai, D., Moore, D.A., Oakes, C.S., Yui, M., 2000. Thermodynamic model for the solubility of thorium dioxide in the Na^+-Cl^--OH^--H_2O system at 23 °C and 90 °C. Radiochim. Acta 88, 297–306.
Ravel, B., Newville, M., 2005. ATHENA, artemis, hephaestus: data analysis for X-ray absorption spectroscopy using IFEFFIT. J. Sinchrotron Rad. 12, 537–541.
Rothe, J., Altmaier, M., Dagan, R., Dardenne, K., Fellhauer, D., Gaona, X., González-Robles, E., Herm, M., Kvashnina, K.O., Metz, V., Pidchenko, I., Schild, D., Vitova, T., Geckeis, H., 2019. Fifteen years of radionuclide Research at the KIT synchrotron source in the context of the nuclear waste disposal safety case. Geosciences 9.
Rothe, J., Butorin, S., Dardenne, K., Denecke, M.A., Kienzler, B., Löble, M., Metz, V., Seibert, A., Steppert, M., Vitova, T., Walther, C., Geckeis, H., 2012. The INE-beamline for actinide science at ANKA. Rev. Sci. Instrum. 83.
Rothe, J., Denecke, M.A., Neck, V., Müller, R., Kim, J.I., 2002. XAFS investigation of the structure of aqueous thorium(IV) species. Inorg. Chem. 41, 249–258.
Rothe, J., Walther, C., Denecke, M.A., Fanghänel, T., 2004. XAFS and LIBD investigation of the formation and structure of colloidal Pu(IV) hydrolysis products. Inorg. Chem. 43, 4708–4718.
Scherrer, P., 1918. Nachrichten von der Gesellschaft der Wissenschaften zu Göttingen. Mathematisch-Physikalische Klasse 2, 98–100.
Sekulić, A., Furić, K., Tonejc, A., Tonejc, A.M., Stubicar, M., 1997. Determination of the monoclinic, tetragonal and cubic phases in mechanically alloyed ZrO_2-Y_2O_3 and ZrO_2-CoO powder mixtures by Raman spectroscopy. J. Mater. Sci. Lett. 16, 260–262.
Shannon, R.D., 1976. Revised effective ionic radii and systematic studies of interatomie distances in halides and chaleogenides. Acta Crystallogr. A32, 751–767.
Sharma, G., Ushakov, S.V., Navrotsky, A., 2018. Size driven thermodynamic crossovers in phase stability in zirconia and hafnia. J. Am. Ceram. Soc. 101, 31–35.
Sheikhattar, M., Attar, H., Sharafi, S., Carty, W.M., 2016. Influence of surface crystallinity on the surface roughness of different ceramic glazes. Mater. Char. 118, 570–574.
Sirotinkin, V.P., Podzorova, L.I., Il'icheva, A., 2022a. Comparative X-ray diffraction study of the Yb_2O_3 stabilized zirconia ceramics doped with SrO and CaO. Mater. Chem. Phys. 277.
Sirotinkin, V.P., Podzorova, L.I., Mikhailina, N.A., kova, Pen, 2022b. X-Ray diffraction study of structural changes in high-strength ceramics based on zirconium oxide with additions of ytterbium and neodymium oxides after hydrothermal treatment. Crystallogr. Rep. 67, 278–285.
Sobol, A.A., Voronko, Y.K., 2004. Stress-induced cubic–tetragonal transformation in partially stabilized ZrO_2: Raman spectroscopy study. J. Phys. Chem. Solid. 65, 1103–1112.
Štefanić, G., Musić, S., Gržeta, B., Popović, S., Sekulić, A., 1998. Influence of pH on the stability of low temperature t-ZrO_2. J. Phys. Chem. Solid. 59, 879–885.
Štefanić, G., Musić, S., Molčanov, K., 2005. The crystallization process of HfO_2 and ZrO_2 under hydrothermal conditions. J. Alloys Compd. 387, 300–307.
Štefanić, G., Popović, S., Musić, S., 1997. Influence of pH on the hydrothermal crystallization kinetics and crystal structure of ZrO_2. Thermochim. Acta 303, 31–39.
Stubican, V.S., Ray, S.P., 1977. Phase equilibria and ordering in the system ZrO_2-CaO. J. Am. Ceram. Soc. 60, 534–537.
Tolborg, K., Walsh, A., 2023. Exploring the high-temperature stabilization of cubic zirconia from anharmonic lattice dynamics. Cryst. Growth Des. 23, 3314–3319.
Trügler, A., Tinguely, J.-C., Krenn, J.R., Hohenau, A., Hohenester, U., 2011. Influence of surface roughness on the optical properties of plasmonic nanoparticles. Phys. Rev. B 83.
Vaitkus, A., Merkys, A., Gražulis, S., 2021. Validation of the Crystallography open database using the crystallographic information framework. J. Appl. Crystallogr. 54, 661–672.
Yashima, M., Arashi, H., Kakihana, M., Yoshimura, M., 1994. Raman scattering study of cubic-tetragonal phase transition in $Zr_{1-x}Ce_xO_2$, solid solution. J. Am. Ceram. Soc. 77, 1067–1071.
Yeryukov, N.A., Milekhin, A.G., Sveshnikova, L.L., Duda, T.A., Pokrovsky, L.D., Gutakovskii, A.K., Batsanov, S.A., Rodyakina, E.E., Latyshev, A.V., Zahn, D.R.T., 2014. Synthesis and characterization of Cu_xS (x = 1−2) nanocrystals formed by the Langmuir−Blodgett technique. J. Phys. Chem. C 118, 23409–23414.
Zimina, A., Dardenne, K., Denecke, M.A., Doronkin, D.E., Huttel, E., Lichtenberg, H., Mangold, S., Pruessmann, T., Rothe, J., Spangenberg, T., Steininger, R., Vitova, T., Geckeis, H., Grunwaldt, J.-D., 2017. CAT-ACT-A new highly versatile x-ray spectroscopy beamline for catalysis and radionuclide science at the KIT synchrotron light facility ANKA. Rev. Sci. Instrum. 88.